Grey-zone simulations of shallow-to-deep convection transition using dynamic subgrid-scale turbulence models

Received: 4 January 2024 | Revised: 9 May 2024 | Accepted: 4 June 2024

DOI: 10.1002/qj.4817

Quarterly Journal of the Royal Meteorological Society RMetS

RESEARCH ARTICLE

Grey-zone simulations of shallow-to-deep convection transition using dynamic subgrid-scale turbulence models

Georgios A. Efstathiou[1] | **Robert S. Plant**[2] | **Fotini Katopodes Chow**[3]

[1]Department of Mathematics and Statistics, University of Exeter, Exeter, UK

[2]Department of Meteorology, University of Reading, Reading, UK

[3]Department of Civil and Environmental Engineering, University of California, Berkeley, California, USA

Correspondence
Georgios A. Efstathiou, Department of Mathematics and Statistics, University of Exeter, Exeter, EX4 4QF, UK.
Email: g.efstathiou@exeter.ac.uk

Funding information
Natural Environment Research Council, Grant/Award Numbers: NE/T011351/1, NE/X018164/1

Abstract

We examine the ability of two dynamic turbulence closure models to simulate the diurnal development of convection and the transition from dry to shallow cumuli and then to deep convection. The dynamic models are compared with the conventional Smagorinsky scheme at a range of cloud-resolving and grey-zone resolutions. The dynamic schemes include the Lagrangian-averaged, scale-dependent dynamic Smagorinsky model and a Lagrangian-averaged, dynamic mixed model. The conventional Smagorinsky model fails to reproduce the shallow convection stage beyond the large-eddy simulation regime, continuously building up the convective available potential energy that eventually leads to an unrealistic deep convection phase. The dynamic Smagorinsky model significantly improves the representation of shallow and deep convection; however, it exhibits issues similar to the conventional scheme at coarser resolutions. In contrast, the dynamic mixed model closely follows the large-eddy simulation results across the range of sub-kilometre simulations. This is achieved by the combined effect of an adaptive length scale and the inclusion of the Leonard terms, which can produce counter-gradient fluxes through the backscatter of energy from the subgrid to the resolved scales and enable appropriate non-local contributions. A further sensitivity test on the inclusion of the Leonard terms on all hydrometeor fluxes reveals the strong interaction between turbulent transport and microphysics and the possible need for further optimisation of the dynamic mixed model coefficients together with the microphysical representation.

KEYWORDS

deep convection, dynamic mixed model, dynamic Smagorinsky, grey zone, LBA, transition, turbulence closure

1 | INTRODUCTION

The representation of the diurnal cycle of convection remains an open problem in numerical weather prediction (NWP) and climate simulations, especially over land (Bechtold *et al.*, 2004; Krishna *et al.*, 2021). Models tend to misrepresent the timing of convection initiation and maximum rainfall (Krishnamurti *et al.*, 2007; Yuan *et al.*, 2013), sometimes even missing the shallow convection stage completely and moving straight to the deep convection phase. These issues are especially acute over tropical regions (Chakraborty, 2010), where the diurnal cycle of convection is the dominant mode of weather variability. Conventional cumulus parametrisations exacerbate the aforementioned issues by exhibiting significant intermittency and sensitivity to their closure parameters, such as the entrainment/detrainment and triggering formulations (Kidd *et al.*, 2013; Yuan *et al.*, 2013).

The large-eddy simulation (LES) utilises very fine resolution grids to capture the large (dominant) turbulence structures in the flow field while parametrising the isotropic (smaller) ones. LES has been shown to accurately simulate shallow cumulus and deep convection cases (Brown, 1999; Brown *et al.*, 2002; Griewank *et al.*, 2020; Gu *et al.*, 2020; Matheou *et al.*, 2011; Petch *et al.*, 2002) as well as the transition from shallow to deep convection (Grabowski *et al.*, 2006). Nonetheless, LES has been mostly used for process studies as it requires high spatial resolution to resolve the inertial subrange of turbulence, and large domains to capture the full scale of the atmospheric circulations involved, especially for deep convection simulations.

NWP models are traditionally run in the Reynolds-averaged Navier–Stokes (RANS) regime, which assumes a clear separation between the "large-scale" environment and the turbulent motions that remain unresolved. Turbulence in RANS is represented in a statistical sense as an ensemble average of different flow realisations. Therefore, boundary-layer (BL) parametrisations should represent the effects of local mixing and non-local transport in the BL, whereas a convective parametrisation is necessary to account for the sources/sinks of heat and moisture due to deep convective cloud formation. Furthermore, some models incorporate a separate shallow convection scheme that parametrises the impact of shallow cumulus development on the simulations, and higher order BL models (e.g. Nakanishi & Niino, 2009) can include a partial-condensation scheme to account for the effects of subgrid clouds on buoyancy fluxes, using predicted or diagnosed turbulence statistics.

The introduction of "convention-permitting" models (i.e., kilometre-scale simulations without or with much weakened convective parametrisations) has provided a step-change in our ability to predict deep convection and subsequent heavy rainfall events (Clark *et al.*, 2016), while also leading to improvements in climate predictions (Schär *et al.*, 2020). This is mostly attributed to the better accuracy of model dynamics at ∼1 km resolutions compared with the errors imposed by conventional convection parametrisations. Increasing the spatial resolution of numerical models further to sub-kilometre scales leads to the development of cloud-resolving models (CRMs) that are able to resolve most of the cloud circulations, especially in deep convection simulations. However, this further grid refinement does not always come with analogous improvement in the rainfall forecast skill, at least compared to the improvements seen in convection permitting models (Ito *et al.*, 2017). In addition, resolved flow becomes overly sensitive to the treatment of turbulent mixing (Beare, 2014). Hanley *et al.* (2015) identified that the subgrid turbulence mixing length controlled the morphology of storms in sub-kilometric simulations with smaller values resulting in smaller-scale cloud cells. Moreover, Verrelle *et al.* (2015) showed that the significant lack of turbulent mixing in deep convective clouds leads to non-converging behaviour of cloud characteristics across a range of CRM resolutions.

Nonetheless, as models push into the sub-kilometre regime, they start to partially resolve the turbulent structures in clouds and the convective BL (CBL). The partially-resolved thermals are very sensitive to the treatment of subgrid mixing (Beare, 2014), while the traditional RANS or LES approaches to turbulence modelling are no longer valid. Therefore, meteorological modelling enters a "grey zone" (Wyngaard, 2004) where there is a lack of knowledge concerning the treatment of unresolved turbulent motion and its effect on resolved dynamics. The grey zone is encountered when the scale of dominant turbulent eddies Λ is comparable to the grid spacing ($\Lambda \sim \Delta$), (Rai *et al.*, 2019; Wyngaard, 2004). Beare (2014) defined the grey zone regime where $\Lambda \sim l_d$ with l_d a dissipation length scale that accounts for the effects of numerical and subgrid (physical) diffusion. In this way the grey zone is established when the model "effective resolution" comes into play. These definitions mean that the grey zone depends on the Λ/Δ ratio (or Λ/l_d) and not the chosen horizontal resolution (Honnert *et al.*, 2011). Hence, any given simulation could transition through multiple grey zones in time and space (see Chow *et al.*, 2019), such as the convective parametrisation grey zone ($O \sim 1$ km), the BL grey zone ($O \sim 100$ m), or near the surface or inversion for LES ($O \sim 10$ m). Even though CRMs are used for benchmark simulations, they are not immune from the ramifications of grey-zone turbulence modelling, as will be shown later in this study.

Recent improvements in high-performance computing allow NWP models to operate in the grey zone. For

this reason, a number of approaches have been developed (Honnert *et al.*, 2020). These methods aim to extend the use of RANS approaches into the grey-zone regime, usually blending between the conventional one-dimensional BL schemes and three-dimensional (3D) LES parametrisation (Boutle *et al.*, 2014; Goger *et al.*, 2018; Shin & Hong, 2015) or modifying mass flux terms to account for the presence of resolved fluxes (Lancz *et al.*, 2018). In addition, closures based on the prognostic turbulence kinetic energy equation have been suggested where the master turbulence length scale is blended between an LES grid-dependent formulation and the mesoscale limit where it is related to the dominant length scales of turbulence (Kurowski & Teixeira, 2018; Zhang *et al.*, 2018).

On the other hand, dynamic turbulence modelling emerges from the LES regime and is based on the Germano identity (Germano *et al.*, 1991), which utilises the smallest resolved turbulent eddies to derive dynamically the closure parameters (i.e., subgrid turbulence length scales) of turbulence models. Efstathiou *et al.* (2018) extended the use of a scale-dependent, Lagrangian-averaged, dynamic Smagorinsky (LASD) model (Bou-Zeid *et al.*, 2005) into the grey zone to simulate an evolving CBL. The dynamic approach significantly improved the BL representation compared to the conventional Smagorinsky (Smagorinsky, 1963) especially in the near-grey-zone regime. Furthermore, Efstathiou (2023) showed that LASD with a dynamic Prandtl number (Pr), was able to capture the diurnal development of shallow cumulus convection by better reproducing the turbulent transport in the BL and cloud layer at a range of grey-zone resolutions. However, as horizontal resolution extends further into the grey zone and the resolved field is only marginally resolved, the eddy-viscosity, stand-alone dynamic schemes reach their usability limit as they cannot produce non-local fluxes that dominate the CBL and cloud development (see Efstathiou, 2023).

Mixed schemes have been introduced to account for the extra terms that arise from the 3D spatially filtered subgrid stress decomposition where RANS rules do not apply (Zang *et al.*, 1993). Mixed models incorporate a Smagorinsky closure together with a scale-similarity term (Bardina *et al.*, 1983) that is related to the Leonard terms (Germano, 1986) and is able to provide backscatter (i.e., reverse the energy flow from the subgrid to the resolved scales), breaking the purely dissipative nature of the SMAG scheme. Moreover, dynamic mixed models have been proposed initially for engineering applications to avoid the ad hoc specification of closure parameters, leading to better adaptation to the resolved field and consequently improving the simulation of complex flows compared with their static counterparts (Anderson & Meneveau, 1999; Zang *et al.*, 1993). In meteorological modelling, mixed models have been introduced to improve the problematic representation of momentum and scalar fluxes in the grey zone (Hanley *et al.*, 2019; Moeng *et al.*, 2010; Strauss *et al.*, 2019; Verrelle *et al.*, 2017) but exhibited sensitivity to the choice of model parameters (see Verrelle *et al.*, 2017). Recent work has examined the beneficial behaviour of dynamic mixed models compared with conventional turbulence schemes in the simulation of stratocumulus (Shi *et al.*, 2018) and deep convection (Shi *et al.*, 2019), mainly due to the ability of the Leonard terms to represent the counter-gradient fluxes while reducing the local contribution of the SMAG model.

Here, we introduce a Lagrangian-averaged dynamic mixed model in the Met Office/NERC Cloud (MONC) model (Brown *et al.*, 2015), which together with LASD is used to simulate the transition from shallow to deep convection over the Amazon during the Large-Scale Biosphere–Atmosphere (LBA) experiment in Amazonia, Brazil campaign (Betts *et al.*, 2002). Even though similar dynamic approaches have been employed in the engineering community, the simulation of shallow and deep moist convection is fundamentally different due to the strong effects of buoyancy, counter-gradient transport, condensation, latent heating, and the complex microphysical process associated with deep convection that take place in an environment that is not uniformly turbulent. Additionally, most of the atmospheric moist convection applications for a dynamic Smagorinsky scheme have been focused on stratocumulus LES (Kirkpatrick *et al.*, 2006; Stevens *et al.*, 2005). The chosen case represents the development of a dry convective CBL that gives rise to a widespread shallow cumulus phase and then transitions to weakly organised deep convection. This test case is surface driven with large-scale forcing based on the set-up of Grabowski *et al.* (2006). An LES of the LBA case study at high resolution will serve as a benchmark simulation. The dynamic approaches will be compared against the conventional Smagorinsky scheme at a range of cloud-resolving and grey-zone resolutions to examine their ability to reproduce the shallow-to-deep convection transition. Moreover, a sensitivity test examining the impact of the Leonard terms on water species transport is presented. This identifies the strong interaction between microphysics and the subgrid-scale (SGS) scheme and highlights a possible need for further optimisation of the mixed model parameters.

2 | TURBULENCE MODELLING

The SGS momentum stress tensor τ_{ij} represents the effects of smaller scale, unresolved turbulent motions on momentum transport and is expressed as

$$\tau_{ij} = \rho_0\left(\overline{u_i u_j} - \overline{u}_i \overline{u}_j\right), \tag{1}$$

where the overbar denotes a spatial filter that partitions between the resolved and SGS flow field, and ρ_0 is a reference density (assuming an anelastic system). The choice of applying a spatial filter to the velocity field u_i conceptually implies an LES modelling approach where the SGS stress, induced by the unresolved turbulent fluctuations, is modelled using a turbulence closure scheme. Further decomposing Equation (1) in terms of resolved and SGS counterparts using $u_i = \overline{u}_i + u_i'$ leads to (see Germano, 1986; Zang *et al.*, 1993)

$$\tau_{ij} = \mathcal{L}_{ij}^{\mathrm{m}} + \mathcal{C}_{ij}^{\mathrm{m}} + \mathcal{R}_{ij}^{\mathrm{m}}. \tag{2}$$

The terms comprising the τ_{ij} are $\mathcal{L}_{ij}^{\mathrm{m}}$ the modified Leonard, $\mathcal{C}_{ij}^{\mathrm{m}}$ the cross terms, and $\mathcal{R}_{ij}^{\mathrm{m}}$ the Reynolds terms, and these include contributions from both resolved and unresolved scales. The modified terms are Galilean invariant (Germano, 1986) and are expressed as

$$\mathcal{L}_{ij}^{\mathrm{m}} = \rho_0\left(\overline{\overline{u}_i\overline{u}_j} - \overline{\overline{u}}_i\overline{\overline{u}}_j\right), \tag{3}$$

$$\mathcal{C}_{ij}^{\mathrm{m}} = \rho_0\left(\overline{\overline{u}_i u_j' + u_i'\overline{u}_j} - (\overline{\overline{u}}_i\overline{u'}_j + \overline{u'}_i\overline{\overline{u}}_j)\right), \tag{4}$$

and

$$\mathcal{R}_{ij}^{\mathrm{m}} = \rho_0\left(\overline{u_i'u_j'} - \overline{u'}_i\overline{u'}_j\right). \tag{5}$$

Note that, in the RANS limit, Equation (2) reduces to $\tau_{ij} = \rho_0\overline{u_i'u_j'}$.

2.1 | Smagorinsky scheme

The Smagorinsky scheme (Lilly, 1967; Smagorinsky, 1963) is an eddy-viscosity scheme that models τ_{ij} in a purely dissipative downgradient form, aiming to reproduce the cascade of energy from the production to the dissipation scales in the inertial subrange of the turbulent kinetic energy spectrum. The deviatoric part of the stress tensor is given by

$$\tau_{ij} = -2\rho_0\nu_{\mathrm{T}}\overline{S}_{ij}f_{\mathrm{m}}(\mathrm{Ri}) \tag{6}$$

with

$$\overline{S}_{ij} = \frac{1}{2}\left(\frac{\partial\overline{u}_i}{\partial x_j} + \frac{\partial\overline{u}_j}{\partial x_i}\right). \tag{7}$$

The overbar denotes resolved quantities (i.e., filtered at the scale Δ) and $f_{\mathrm{m}}(\mathrm{Ri})$ is the stability function for momentum as a function of the Richardson number (Ri). The treatment of stability functions is described in Efstathiou (2023). The eddy viscocity ν_{T} is given by

$$\nu_{\mathrm{T}} = \lambda^2|\overline{S}|, \tag{8}$$

where $|\overline{S}| = (2\overline{S}_{ij}\overline{S}_{ij})^{1/2}$ is the modulus of the strain rate tensor and λ is the SGS mixing length:

$$\lambda = C_{\mathrm{S}}\Delta. \tag{9}$$

In order to control the excessively dissipative nature of the Smagorinsky scheme close to the ground, a wall-damping function was proposed by Mason and Thomson (1992) for λ:

$$\frac{1}{\lambda^2} = \frac{1}{(\kappa z)^2} + \frac{1}{(C_{\mathrm{S}}\Delta)^2}. \tag{10}$$

The default MONC configuration uses $C_{\mathrm{S}} = 0.23$ and $\Delta = \Delta x$, with Δx expressing the horizontal grid spacing and κ the von Kármán constant set to 0.4. Similarly, for the SGS heat flux we have

$$\tau_{\theta j} = -\rho_0\frac{\nu_{\mathrm{T}}}{\mathrm{Pr}}\frac{\partial\overline{\theta}}{\partial x_j}f_{\mathrm{h}}(\mathrm{Ri}), \tag{11}$$

where Pr is the SGS Prandtl number (set equal to 0.7) and $f_{\mathrm{h}}(\mathrm{Ri})$ is the stability function for heat. For the nth SGS water species flux, we likewise have

$$\tau_{q_n j} = -\rho_0\frac{\nu_{\mathrm{T}}}{\mathrm{Pr}}\frac{\partial\overline{q}_n}{\partial x_j}f_{\mathrm{h}}(\mathrm{Ri}). \tag{12}$$

2.2 | Lagrangian-averaged, scale-dependent dynamic Smagorinsky

The LASD Smagorinsky model used in this study follows the implementation of Efstathiou (2023) in MONC, based on the work of Bou-Zeid *et al.* (2005), and is only described briefly here. The dynamic approach uses the Germano identity (Germano *et al.*, 1991), which relates the stresses at two different scales with the fluxes at their intermediate scales to calculate a flow-dependent C_{S}:

$$L_{ij} = T_{ij} - \widetilde{\tau}_{ij} = \widetilde{\overline{u}_i\overline{u}_j} - \widetilde{\overline{u}}_i\widetilde{\overline{u}}_j, \tag{13}$$

where the tilde denotes explicit test-filtering at the scale of 2Δ, T_{ij} is the SGS stress tensor model applied at the same scale, and L_{ij} is the resolved stress tensor associated with scales intermediate between Δ and 2Δ. Note that ρ_0 has been dropped from all terms in Equation (13) as a constant factor. Applying the Smagorinsky model, Equation (6), in Equation (13) at scale 2Δ results in

$$L_{ij} = C_{\mathrm{S}(2\Delta)}^2 M_{ij}, \tag{14}$$

with

$$M_{ij} = 2\Delta^2[|\overline{S}|\widetilde{\overline{S}_{ij}f_{\mathrm{m}}}(\mathrm{Ri}) - 4\beta|\widetilde{\overline{S}}|\widetilde{\overline{S}}_{ij}f_{\mathrm{m}}(\widetilde{\mathrm{Ri}})]. \tag{15}$$

Minimising the squared error of Equation (14) as in Lilly (1992) leads to

$$C_{\mathrm{S}(2\Delta)}^2 = \frac{\langle L_{ij}M_{ij}\rangle}{\langle M_{ij}M_{ij}\rangle}. \tag{16}$$

The angle brackets represent Lagrangian averaging as in Efstathiou (2023) and Bou-Zeid *et al.* (2005), and based on Meneveau *et al.* (1996).

Similarly at scales 4Δ (Bou-Zeid *et al.*, 2005; Porté-Agel *et al.*, 2000) we have

$$C^2_{S(4\Delta)} = \frac{\langle Q_{ij} N_{ij} \rangle}{\langle N_{ij} N_{ij} \rangle}, \tag{17}$$

where

$$Q_{ij} = \widehat{\overline{u}_i \overline{u}_j} - \hat{\overline{u}}_i \hat{\overline{u}}_j \tag{18}$$

and

$$N_{ij} = 2\Delta^2 [|\overline{S}| \widehat{\overline{S}_{ij} f_m(\mathrm{Ri})} - 16\beta^2 |\hat{\overline{S}}| \hat{\overline{S}}_{ij} f_m(\hat{\mathrm{Ri}})], \tag{19}$$

with the caret denoting filtering at the scale 4Δ.

The parameter β introduces scale dependency to the dynamic model (Bou-Zeid *et al.*, 2005) and is calculated using

$$\beta = \max \left[\frac{C^2_{S(4\Delta)}}{C^2_{S(2\Delta)}}, 0.125 \right], \tag{20}$$

where a minimum value is set to avoid numerical instabilities when β tends to zero (see Bou-Zeid *et al.*, 2005). The Smagorinsky coefficient used at the grid scale—in Equation (8) without the use of Equation (10)—is obtained from

$$C^2_S = \frac{C^2_{S(2\Delta)}}{\beta}. \tag{21}$$

A basic assumption behind LASD is that applying the Germano identity at the two scales yields C_S values that are more representative of each of the filtered scales (see Equations 16 and 17) than the grid scale (see Bou-Zeid *et al.*, 2005). This implies that β is initially set equal to one in Equations 15 and 19.

2.2.1 | Dynamic model for the SGS Prandtl number

The Germano identity can be applied again in the heat flux equation, Equation (11), to derive the SGS Pr through the coefficient $C_\theta = C^2_S / \mathrm{Pr}$ as

$$C_{\theta(2\Delta)} = \frac{\langle H_j R_j \rangle}{\langle R_j R_j \rangle}, \tag{22}$$

for scales 2Δ, with R_j given by

$$R_j = \Delta^2 \left(|\overline{S}| \widetilde{\frac{\partial \overline{\theta}}{\partial x_j}} f_h(\mathrm{Ri}) - 4\beta_\theta |\widetilde{\overline{S}}| \widetilde{\frac{\partial \overline{\theta}}{\partial x_j}} f_h(\widetilde{\mathrm{Ri}}) \right), \tag{23}$$

and

$$H_j = T_{\theta j} - \widetilde{\tau}_{\theta j} = \widetilde{\overline{u}_j \overline{\theta}} - \widetilde{\overline{u}}_j \widetilde{\overline{\theta}}. \tag{24}$$

For scales 4Δ we have respectively

$$C_{\theta(4\Delta)} = \frac{\langle F_j X_j \rangle}{\langle X_j X_j \rangle} \tag{25}$$

and

$$F_j = \widehat{\overline{u}_j \overline{\theta}} - \hat{\overline{u}}_j \hat{\overline{\theta}}, \tag{26}$$

with

$$X_j = \Delta^2 \left(|\overline{S}| \widehat{\frac{\partial \overline{\theta}}{\partial x_j}} f_h(\mathrm{Ri}) - 16\beta^2_\theta |\hat{\overline{S}}| \widehat{\frac{\partial \overline{\theta}}{\partial x_j}} f_h(\hat{\mathrm{Ri}}) \right). \tag{27}$$

The final C_θ is derived from

$$C_\theta = \frac{C_{\theta(2\Delta)}}{\beta_\theta}, \tag{28}$$

where the scale dependency parameter β_θ is calculated analogously to Equation (20):

$$\beta_\theta = \max \left[\frac{C_{\theta(4\Delta)}}{C_{\theta(2\Delta)}}, 0.125 \right]. \tag{29}$$

2.3 | Lagrangian averaged dynamic mixed model

The Germano identity relates the smallest resolved scales of turbulent motion to the SGS fluxes in order to optimise the model's closure parameters, expressing a form of scale similarity between the two. A turbulence model that utilises a more direct form of scale similarity is the Mixed Model (MM) as presented in Bardina *et al.* (1983). The MM assumes that the most important scales of interaction that dominate the subsequent SGS energy dissipation lie between the smallest resolved and the "largest" unresolved turbulent eddies by introducing a scale similarity term together with the Smagorinsky model. Zang *et al.* (1993) introduced a dynamic version of the MM (DMM), where the anisotropic part of the SGS tensor is given by

$$\tau_{ij} = -2\rho_0 (C_S \Delta)^2 |\overline{S}| \overline{S}_{ij} f_m(\mathrm{Ri}) + \rho_0 C_n \mathcal{L}^m_{ij}. \tag{30}$$

Hence, the MM explicitly accounts for the Leonard terms (see Germano, 1986) and models the $\mathcal{C}^m_{ij}$—as shown in Equation (4)—and $\mathcal{R}^m_{ij}$, Equation (5), using the Smagorinsky model. Zang *et al.* (1993) specified $C_n = 1$.

In this study, we implement the DMM version of Anderson and Meneveau (1999) which in turn is based on

the analysis of Liu *et al.* (1994). The SGS scale tensor is modelled by:

$$\tau_{ij} = -2\rho_0(C_S\Delta)^2|\overline{S}|\overline{S}_{ij}f_m(\mathrm{Ri}) + \rho_0 C_n(\widetilde{\overline{u}_i\overline{u}_j} - \widetilde{\overline{u}}_i\widetilde{\overline{u}}_j). \quad (31)$$

The main difference between the two versions (Equations 30 and 31) is that Equation (31) uses filtering at scales of 2Δ as denoted by the tilde in Equation (13). Thus, the Leonard term at scale Δ is approximated based on the equivalent term at scales intermediate between Δ and 2Δ. Applying the proposed model, Equation (31), at scales 2Δ results in

$$T_{ij} = -2\rho_0 C^2_{S(2\Delta)}(2\Delta)^2|\widetilde{\overline{S}}|\widetilde{\overline{S}}_{ij}f_m(\widetilde{\mathrm{Ri}}) + \rho_0 C_n(\widehat{\widetilde{\overline{u}_i}\widetilde{\overline{u}}_j} - \widehat{\widetilde{\overline{u}}}_i\widehat{\widetilde{\overline{u}}}_j), \quad (32)$$

which follows the form of the similarity terms suggested by Liu *et al.* (1994). Here, we also set $C_n = 1$ (see also Shi *et al.*, 2018, 2019) and assume a scale invariant form of the DMM, which means that $C_S = C_{S(2\Delta)}$. These choices will be revisited and discussed in concluding the article. Minimising the squared error of the Germano identity under this model results in

$$C_S^2 = \frac{\langle L_{ij}M_{ij}\rangle - \langle Z_{ij}M_{ij}\rangle}{\langle M_{ij}M_{ij}\rangle}, \quad (33)$$

with (see Anderson & Meneveau, 1999)

$$Z_{ij} = (\widehat{\widetilde{\overline{u}_i}\widetilde{\overline{u}}_j} - \widehat{\widetilde{\overline{u}}}_i\widehat{\widetilde{\overline{u}}}_j) - (\widetilde{\overline{u}_i\overline{u}_j} - \widetilde{\overline{u}}_i\widetilde{\overline{u}}_j), \quad (34)$$

where the angle brackets denote Lagrangian averaging of the contracted tensors as in LASD (dropping the ρ_0 factor as mentioned earlier). We also tentatively adopt the same time-scale formulation used in LASD (see Bou-Zeid *et al.*, 2005; Efstathiou, 2023). Negative C_S values are clipped to zero as the Smagorinsky part of the model is assumed to be purely dissipative. The similarity terms can provide "backscatter"; that is, reverse the flow of energy from the subgrid to the resolved scales. It should be recognized that even though the model is scale invariant the C_S derivation here includes information from the 4Δ scales through the filtered similarity terms in Equation (34).

2.3.1 | DMM for scalar transport

The DMM is also used to model the SGS heat flux as

$$\tau_{\theta j} = -\rho_0 C_\theta|\overline{S}|\frac{\partial\overline{\theta}}{\partial x_j}f_h(\mathrm{Ri}) + \rho_0 C_{n\theta}(\widetilde{\overline{u}_j\overline{\theta}} - \widetilde{\overline{u}}_j\widetilde{\overline{\theta}}) \quad (35)$$

and the nth water species

$$\tau_{q_{nj}} = -\rho_0 C_\theta|\overline{S}|\frac{\partial\overline{q}_n}{\partial x_j}f_h(\mathrm{Ri}) + \rho_0 C_{n\theta}(\widetilde{\overline{u}_j\overline{q}_n} - \widetilde{\overline{u}}_j\widetilde{\overline{q}}_n). \quad (36)$$

The scale-invariant C_θ is then derived using Equation (24) (Germano identity) as (assuming $C_{n\theta} = 1$):

$$C_\theta = \frac{\langle H_jR_j\rangle - \langle K_jR_j\rangle}{\langle R_jR_j\rangle}, \quad (37)$$

with

$$K_j = (\widehat{\widetilde{\overline{u}_j}\widetilde{\overline{\theta}}} - \widehat{\widetilde{\overline{u}}_j}\widehat{\widetilde{\overline{\theta}}}) - (\widetilde{\overline{u}_j\overline{\theta}} - \widetilde{\overline{u}}_j\widetilde{\overline{\theta}}). \quad (38)$$

As for momentum, angle brackets represent Lagrangian averaging with the same time-scale used for momentum (see also Huang *et al.*, 2008). The dynamically derived C_θ is applied to all scalars, whereas negative values are again set equal to zero.

3 | LBA CASE STUDY AND MODEL SET-UP

The case study follows the set-up of the Grabowski *et al.* (2006) intercomparison and is based on an idealisation of observations from the LBA observational campaign in Amazonia on February 23, 1999. The LBA is a well-established case used by many studies as a benchmark simulation for convective development and shallow to deep convection transition over land (see Böing *et al.*, 2012; Grabowski, 2023; Khairoutdinov & Randall, 2006; Lang *et al.*, 2007). The anelastic simulations performed are forced by varying surface fluxes (sensible and latent) and planar-averaged radiative tendencies. They are initialised by a morning sounding corresponding to the start of the simulation at 0730 h local solar time (UTC - 4 h). The domain size in MONC is set to $76.8 \times 76.8\,\mathrm{km}^2$, which is the largest domain set-up used in Grabowski *et al.* (2006). The domain top is set at 24 km with a vertical grid consisting of 216 points. Vertical resolution remains the same across all simulations with $\Delta z = 50$ m up to 1,500 m above the surface, $\Delta z = 100$ m up to 16 km, and $\Delta z = 200$ m up to model top with a damping layer applied above 16 km. Sensitivity tests with more grid points in the vertical did not reveal any significant differences. The Cloud AeroSol Interactions Microphysics (CASIM) model (Field *et al.*, 2023) is used in a double-moment configuration to predict the number concentration and mixing ratios of liquid water (q_l), ice (q_i), snow (q_s), rain (q_r), and graupel (q_g).

The reference LES is run with a horizontal grid spacing of $\Delta x = 50$ m (resulting in $1{,}536 \times 1{,}536$ horizontal grid points) using the SMAG scheme. According to Bryan *et al.* (2003), a resolution of about 100 m is needed to resolve an inertial subrange of turbulence for deep convection simulations. Additionally, Efstathiou (2023) showed that $\Delta x = 50$ m is adequately converging for the shallow convection Atmospheric Radiation Measurement (ARM)

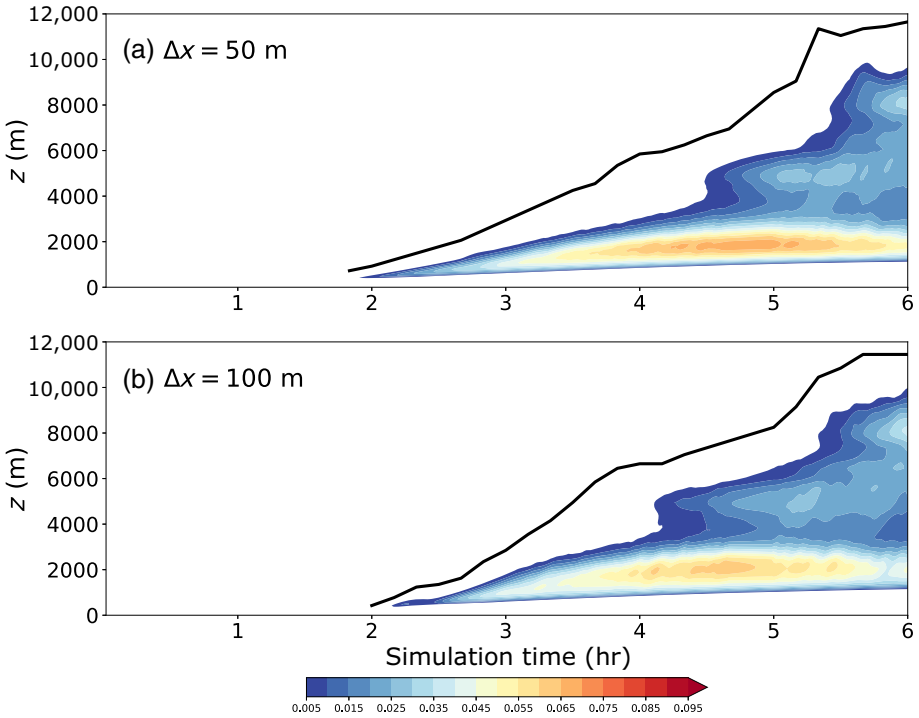

FIGURE 1 Time evolution of planar-averaged total condensate except rain (colour bar in g·kg^{-1}) from the Large-Scale Biosphere–Atmosphere experiment (LBA): (a) large-eddy simulation (LES). ($\Delta x = 50$ m) reference simulation; (b) $\Delta x = 100$ m simulation. The black bold line represents the maximum cloud top height (any grid point where $q_c \geq 10^{-2}$ g·kg^{-1}). The 0°C isotherm is roughly found at 4,700 m.

case (Brown *et al.*, 2002). A simulation with $\Delta x = 100$ m was performed to check for adequate relative convergence of the reference LES and a brief comparison is presented in the Appendix A and Figure 1. Coarser simulations are conducted with $\Delta x = 200$, 400, and 800 m comparing the SMAG with LASD and the DMM in reproducing the transitions from dry to shallow and deep cumulonimbus convection. The DMM is initially applied using the similarity terms only in the momentum and heat flux equations (Equations 31 and 35 respectively), whereas vapour and hydrometeor SGS fluxes are modelled using Equation (12) with the dynamically derived C_θ. In Section 4 we examine the impact on the LBA simulations of including the similarity terms for all hydrometeors.

3.1 | Simulation results

3.1.1 | Convection evolution

The time evolution of planar-averaged condensate except rain (i.e., $q_c = q_l + q_i + q_s + q_g$) from the LES is shown in Figure 1a, together with the maximum cloud top height (any grid point where $q_c \geq 10^{-5}$ g·g^{-1}) for every 600 s snapshot. A well-defined, developing shallow cumulus stage can be identified from about 2 to 4.5 hr after the start of the simulation. The bulk of cloud water extends from about 1 to 3.5 km in height, with maximum cloud tops reaching a mediocris to congestus stage of about 5 km height around 4.5 hr into the simulation. Starting at 4.5 hr, a deep convection phase begins, with cloud tops reaching almost 12 km at the end of the simulation. The LES results presented here are very similar to the Khairoutdinov and Randall (2006) $\Delta x = 100$ m run (which uses a larger domain) in terms of the evolution (and magnitude) of q_c, the timing of the shallow to deep transition and maximum cloud top height—see Khairoutdinov and Randall (2006, Fig. 1). A notable difference is that the planar-averaged q_c top in Figure 1a is somehow lower during the course of the simulation, which is more noticeable at the deep stage, meaning that probably fewer clouds reach the maximum top in our LES. Grabowski *et al.* (2006) found significant differences between models, especially in the simulated cloud mass centre in their intercomparison study that can be further enhanced by differences in resolution, domain size, or microphysical parametrisations (see also Grabowski, 2023). At $\Delta x = 100$ m (Figure 1b), the q_c evolution is quite similar to the LES with slightly higher cloud tops present during the shallow cumulus stage. As will be shown later, the differences between our reference and the $\Delta x = 100$ m run are small (see Appendix A), especially compared with the coarser grey-zone simulations, ensuring sufficient convergence of our LES.

At coarser resolutions, SMAG simulations start to reveal significant discrepancies in the representation of both the shallow and deep convection. Even at $\Delta x = 200$ m (Figure 2a) the SMAG run produces a shorter shallow cumulus phase (onset delayed by 1 hr) with a faster evolving deep stage where the condensate (especially the contributions from snow and graupel; not shown) exhibits

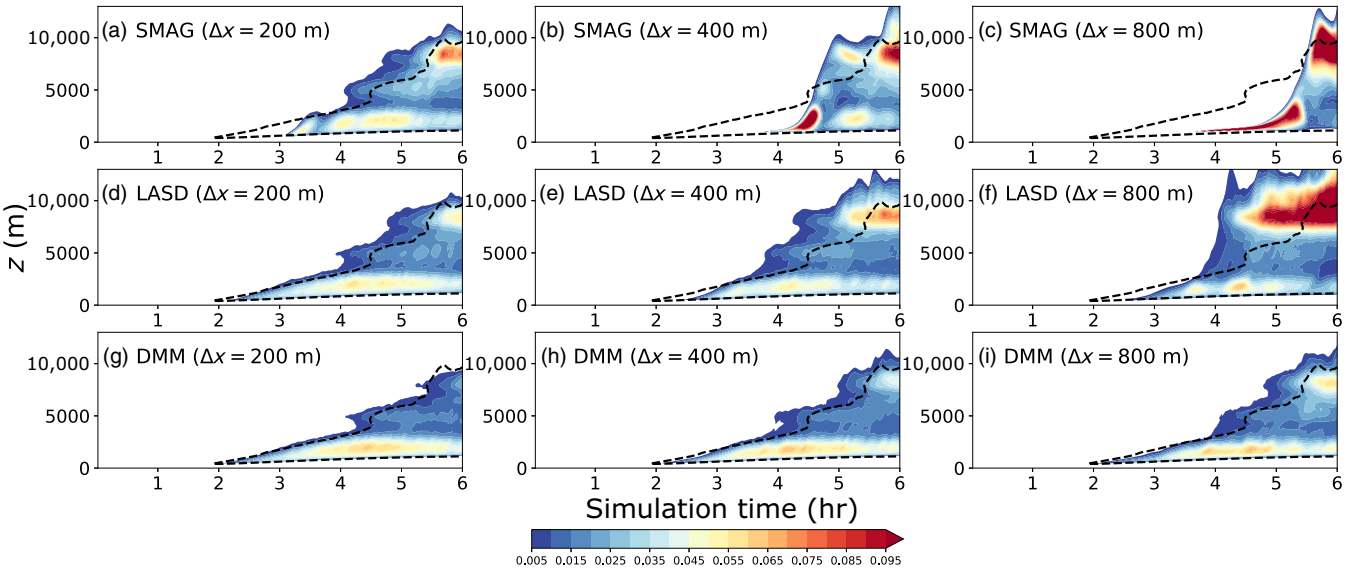

FIGURE 2 Time evolution of planar-averaged total condensate except rain (colour bar in g·kg^{-1}) from (a–c) the conventional Smagorinsky (SMAG) model for (a) $\Delta x = 200$ m, (b) $\Delta x = 400$ m, and (c) $\Delta x = 800$ m, (d–f) the Lagrangian-averaged, dynamic Smagorinsky (LASD) model for (d) $\Delta x = 200$ m, (e) $\Delta x = 400$ m, and (f) $\Delta x = 800$ m, and (g–i) Dynamic Mixed Model (DMM) for (g) $\Delta x = 200$ m, (h) $\Delta x = 400$ m, and (i) $\Delta x = 800$ m Large-Scale Biosphere–Atmosphere experiment (LBA) simulations. The black dashed line shows the 0.005 g·kg^{-1} contour from the large-eddy simulation (LES).

significantly higher mixing ratios compared with the LES (e.g., at 5.5 hr and 8,000 m elevation). The $\Delta x = 400$ and 800 m simulations (Figure 2b,c) almost completely miss the shallow cumulus stage, exhibiting a brief, very shallow layer of excessive condensate (producing almost an overcast scene; not shown) and then go straight to deep convection, which is characterised by excessively high (low) values of condensate in the deep (low) clouds compared with the LES.

Simulations with LASD (Figure 2d–f) substantially improve the development of convection compared with SMAG. The shallow cumulus stage is consistently defined in all simulations even though it is delayed in the 400 and 800 m runs compared with the LES. However, the deep convection stage suffers from the same issues as SMAG, especially at $\Delta x = 800$ m (Figure 2f), with deep overshooting clouds that contain high concentrations of hydrometeors at upper levels.

The DMM results, in contrast, are relatively grid independent, with the planar-averaged condensate evolution being very similar to the LES at all test resolutions (Figure 2g–i). DMM and LASD are fairly close at $\Delta x = 200$ m but DMM outperforms LASD at coarser resolutions. The shallow stage remains largely unchanged across the different resolutions while the deep stage initiates at approximately the right time in comparison with the LES. Nonetheless, some discrepancies with the LES are observed during the deep stage developments at $\Delta x =$ 800 m, where the DMM simulation produces a slightly increased amount of condensate in deep clouds (Figure 2i).

Examining in more detail the mechanisms that influence the evolution of condensate, Figure 3 shows the time evolution of maximum vertical velocity w and mean precipitation rate from the 400 and 800 m simulations compared with the LES. SMAG shows significant delay in the spin-up of resolved motion (about 3 hr in the 400 m and even more in the 800 m simulation) compared with the LES and the dynamic simulations, leading to the observed lack of shallow convection stage in Figure 2b. This same SMAG behaviour has been seen in dry CBL grey-zone simulations (e.g., Efstathiou *et al.*, 2016; Simon *et al.*, 2019) as well as in shallow convection development (Efstathiou, 2023). In addition, the instantaneous instability release when the resolved flow spins up results in a huge spike in the precipitation rate. This is especially prominent in the 800 m simulation (Figure 3d), whereas the 400 m simulation produces two secondary peaks, roughly following the LES but with significantly exaggerated precipitation rates.

The build-up of convective instability in the SMAG simulations, due to the lack of resolved motion and subsequent mixing, can be seen in Figure 4. Convective available potential energy (CAPE) increases in time up to a maximum value that roughly corresponds to the onset of rainfall in the 400 and 800 m SMAG simulations (Figure 3). The 400 m SMAG simulation builds CAPE faster as the CBL profiles become more superadiabatic compared with the 800 m run (see Figures 6a and 7a later), which in turn delays the release of CAPE (Figure 3). In contrast, the LES and the 400 m DMM simulation (as well as all the

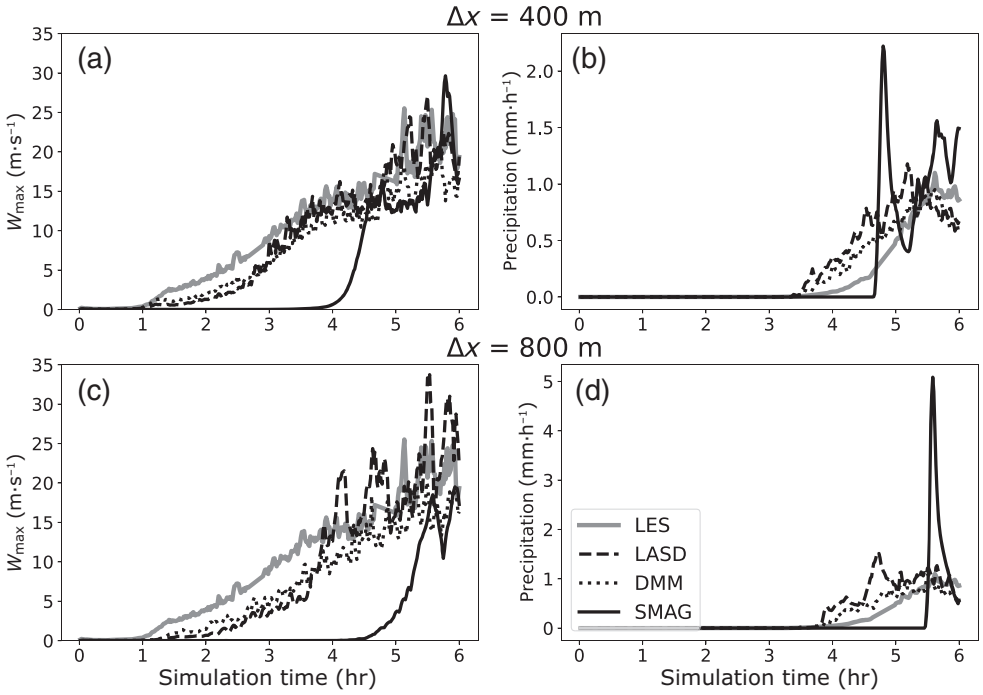

FIGURE 3 Time evolution of (a) maximum vertical velocity at $\Delta x = 400$ m, (b) mean precipitation rate at $\Delta x = 400$ m, (c) maximum vertical velocity at $\Delta x = 800$ m, and (d) mean precipitation rate at $\Delta x = 800$ m from the conventional Smagorinsky (SMAG) model, the Lagrangian-averaged, dynamic Smagorinsky (LASD) model, and the Dynamic Mixed Model (DMM) Large-Scale Biosphere–Atmosphere experiment (LBA) simulations. Note that the scales are different in (b) and (d).

other dynamic runs, but only the 400 m DMM is included in Figure 4) retain near-constant values of CAPE that gradually reduce near the end of the simulations. Moreover, convective clouds in the coarse SMAG simulations exhibit signs of "undiluted" moist thermals, showing a maximum in vertical velocity at 400 m (Figure 3a). In fact, the variance of vertical velocity peaks in the 400 m simulation (not shown), which is almost the same as in the LES, before reducing in the 800 m SMAG run. This can be attributed to the lack of proper entrainment and mixing during cloud development at coarse resolutions as seen in Verrelle *et al.* (2015).

The dynamic runs (LASD and DMM) improve the behaviour of the maximum w evolution from the spin-up of resolved motion to the shallow cumulus and then the deep stage, with delays of about 30 min compared with the LES. This explains the ability of the dynamic approaches to actually capture the shallow cumulus phase compared with SMAG. Precipitation rates follow the LES, with DMM showing better agreement even though rainfall starts slightly earlier and is somewhat stronger in the dynamic simulations. However, at 800 m resolution, LASD exhibits strong maximum w during the deep stage (Figure 3c), which is related to higher precipitation rates and an earlier peak compared with LES and DMM (Figure 3d). The LASD 800 m simulation manifests characteristics similar to the 400 m SMAG simulation with bursts of w and recovery, signalling that there is not enough mixing in the cloud layer during the deep stage of development (Verrelle *et al.*, 2015); however, the impact on the rainfall rates, even though it is evident, is not as pronounced as in SMAG. In contrast,

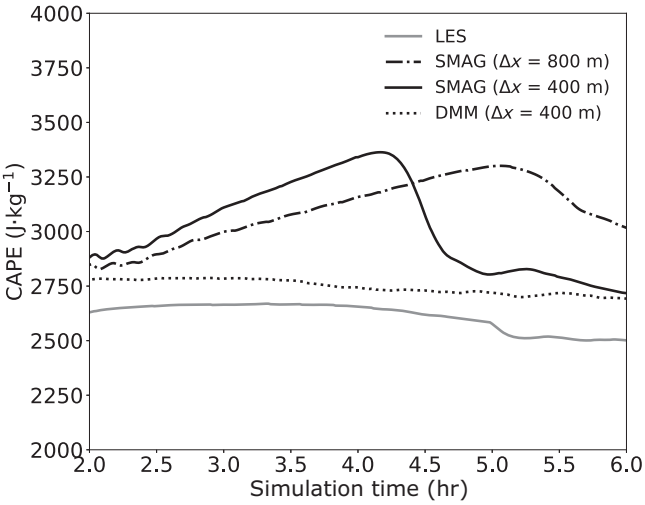

FIGURE 4 Time evolution of convective available potential energy (CAPE) from the $\Delta x = 400$ m and 800 m conventional Smagorinsky (SMAG) model simulations and the large-eddy simulation (LES). The Dynamic Mixed Model (DMM) 400 m CAPE is also presented for comparison.

DMM shows a monotonic decrease of resolved maximum w (and vertical velocity variance in the cloud layer) that results in a smoother evolution and closer agreement with the LES condensate and precipitation evolution across the different resolutions.

Figure 5 shows the time evolution of liquid water path (LWP) and ice water path (IWP) for all simulations. The dynamic runs closely follow the LES LWP evolution at both 400 and 800 m (Figure 5a,c). In contrast, SMAG

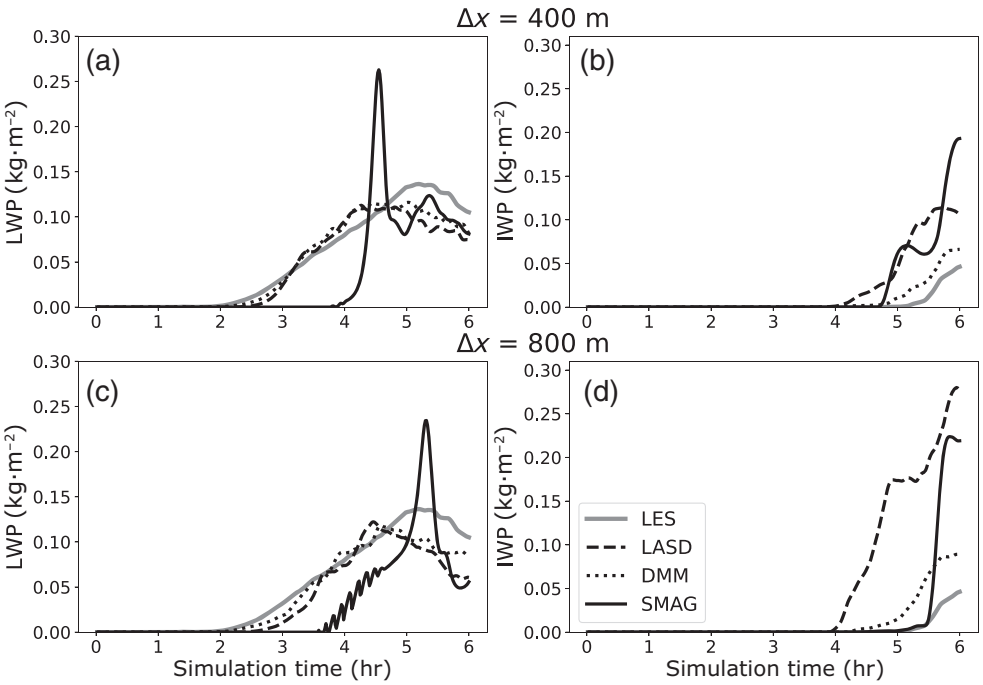

FIGURE 5 Time evolution of (a, c) mean liquid water path (LWP) at (a) $\Delta x = 400$ m and (c) $\Delta x = 800$ m, and (b, d) mean ice water path (IWP) at (b) $\Delta x = 400$ m and (d) $\Delta x = 800$ m from the conventional Smagorinsky (SMAG) model, the Lagrangian-averaged, dynamic Smagorinsky (LASD) model, and the Dynamic Mixed Model (DMM) Large-Scale Biosphere–Atmosphere experiment (LBA) simulations.

shows a peak in LWP that can be also seen in Figure 2b,c, where q_c shows a maximum at around 4 hr after the start of the simulation. It should be noted that the SMAG 800 m simulation displays an oscillatory behaviour during spin-up (Figure 5c) related to the very thin cloud layer at around 4 hr into the run (Figure 2c). Furthermore, the SMAG IWP is excessive in comparison with LES and the dynamic runs at 400 m, in agreement with the condensate content during the deep phase in Figure 2b. The LASD runs start to produce substantially larger amounts of ice condensate (mainly snow) than all other simulations do (Figure 5d). DMM is able to better reproduce the evolution of LWP and IWP, closely following the LES evolution and magnitude at both coarse resolution runs.

3.1.2 | Mean vertical profiles

The vertical structure of the BL, through the planar-averaged profiles of potential temperature, water vapour, and vertical velocity variance, during the shallow cumulus stage ($t = 12{,}600$ s; 3.5 hr from the start of the simulation) and near the end of the simulation when deep convection is fully developed ($t = 21{,}300$ s; ≈6 hr from the start) is depicted in Figures 6 and 7 for the 400 and the 800 m simulations respectively. For the resolved w variance plots (Figures 6c,f and 7c,f) the reference grey line represents the variance of the coarse-grained w LES fields at each target resolution following Honnert *et al.* (2011). The potential temperature (Figure 6a) and water vapour mixing ratio (Figure 6b) profiles during the shallow stage are well reproduced by the dynamic approaches at 400 m resolution in contrast to SMAG, which exhibits superadiabatic potential temperature profiles with a cooler and moister BL. This is attributed to the lack of any resolved overturning motion compared with the dynamic procedures (LASD and DMM) and the coarse-grained LES fields, as seen in Figure 6c (nil vertical velocity variance for SMAG), resulting in the poor ventilation of the BL in SMAG. Efstathiou (2023) identified the same behaviour during the shallow convection development stage, and Singh *et al.* (2021) observed similar effects in the pre-convective BL. By the time the deep convection phase is reached, the SMAG simulation has spun up (see Figure 6f) and roughly matches the LES BL profiles, although the deep convection is too energetic.

The 800 m simulations (in Figure 7) show similar characteristics to the corresponding 400 m simulations, the major difference being that LASD produces a poorer BL representation especially during the deep convection stage (Figure 7d). LASD profiles lie between the SMAG and DMM during the shallow stage (Figure 7a). This is reflected in the time series of maximum w (Figure 3c) and the condensate evolution in Figure 2f. The resolved turbulence energetics, as expressed by the vertical velocity variance, exhibit the slightly overenergetic structure of the BL in the dynamic simulations compared with the coarse-grained LES, this being more pronounced in the 800 m DMM than in the LASD simulation.

Additionally, the planar-averaged heat-flux profiles for the 400 m and 800 m simulations are shown in Figures 8 and 9 respectively. Fluxes from the coarse simulations are also compared with the LES coarse-grained fluxes at 400 and 800 m. During the shallow cumulus stage SMAG does

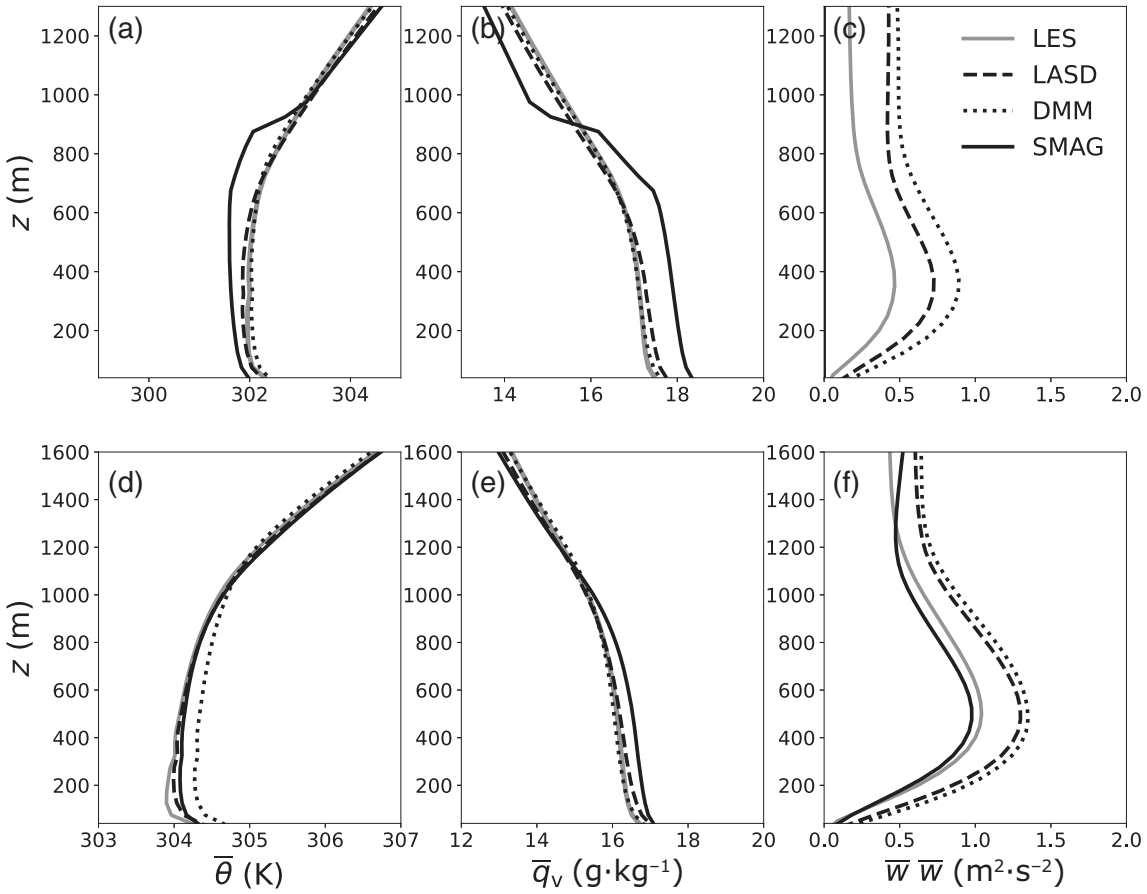

FIGURE 6 Planar-averaged profiles in the boundary layer of (a, d) potential temperature ($\overline{\theta}$), (b, e) water vapour mixing ratio ($\overline{q}_v$), and (c, f) vertical velocity variance ($\overline{w}\,\overline{w}$) during the (a)–(c) shallow cumulus stage and (d)–(f) deep convection phase at $\Delta x = 400$ m from the large-eddy simulation (LES) and conventional Smagorinsky (SMAG) model, the Lagrangian-averaged, dynamic Smagorinsky (LASD) model, and the Dynamic Mixed Model (DMM) simulations. The grey line in (c) and (f) represents the vertical velocity variance of the coarse-grained LES fields at $\Delta x = 400$ m.

not produce any resolved heat fluxes (see also Figures 6e and 7e), relying on the local SGS fluxes (Figures 8b and 9b), and leading to the superadiabatic profiles seen in Figures 6a and 7a. In addition, there are no heat fluxes in the statically stable air above the BL as SMAG misses the shallow cumulus development stage. On the other hand, LASD and DMM can reproduce the total LES fluxes at 400 m (Figure 8c), with LASD producing more energetic resolved flow (Figure 8a) compared with DMM, which compensates the smaller resolved fluxes with positive SGS heat flux in the cloud layer, remaining much closer to the LES partitioning between resolved and SGS fluxes (see Figure 2 for the extent of the cloud layer for each simulation). As suggested by the coarse-grained LES fluxes, there are significant positive fluxes in the cloud layer, especially during the shallow stage (Figures 8b and 9b), implying strong counter-gradient heat transport in clouds. LASD produces almost zero SGS fluxes, similar to the findings of Efstathiou (2023), as C_θ tends to zero (see also Shi *et al.*, 2018). In contrast, DMM is able to produce counter-gradient SGS heat fluxes through the similarity term (see red dotted line in Figures 8b and 9b). The eddy-diffusion part of the model is almost turned off (as in LASD) similar to the findings of Shi *et al.* (2018) and Shi *et al.* (2019). At 800 m LASD produces much stronger resolved and slightly dissipative (negative) SGS fluxes in the cumulus layer, whereas DMM mainly produces positive SGS fluxes on average, better agreeing with the LES. It should be noted that the resolved flow in both LASD and DMM remains overenergetic in the shallow cumulus-topped BL (see Figure 9a).

The heat fluxes in the deep convection stage are dominated by the excessive downgradient diffusion produced by SMAG, especially at 800 m (see also Shi *et al.*, 2019). The dynamic models almost completely turn off the Smagorinsky-type SGS heat fluxes with DMM, retaining positive heat fluxes in the BL through the extra similarity terms that closely follow the coarse-grained

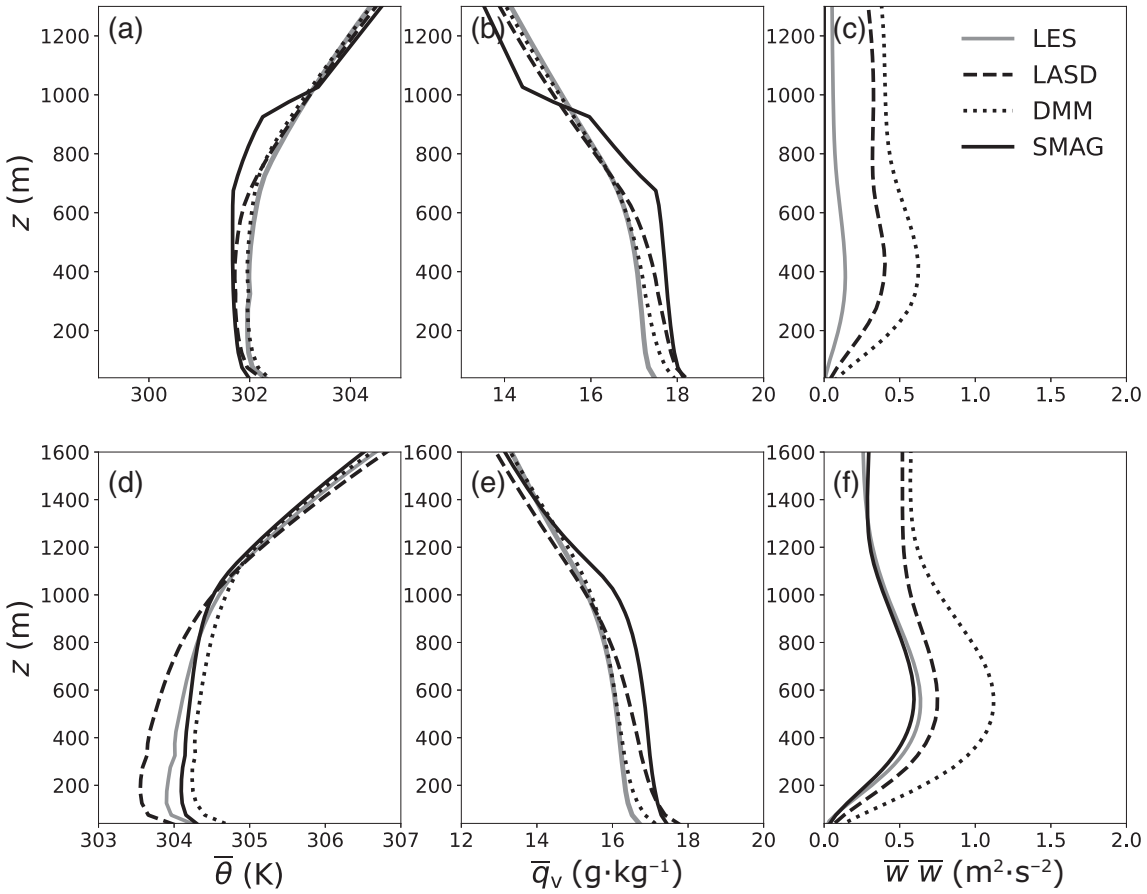

FIGURE 7 Same as Figure 6 but for the $\Delta x = 800$ m simulations.

LES (even though their magnitude is less compared with the coarse-grained fields). At 400 m SMAG produces overenergetic resolved fluxes in the cloud layer compared with the coarse-grained LES (Figure 8d) to compensate for the strong SGS diffusion (Figure 8e). In addition, the resolved heat flux near cloud top is overexcessive compared with the LES, which can also be seen in the condensate time series (Figure 5). LASD captures the total heat (Figure 8f) flux by resolving all flux in the cloud layer, whereas DMM is the only scheme that can reproduce SGS counter-gradient fluxes in the cloud layer.

3.1.3 | Horizontal cross-sections of the thermodynamic BL structure

Khairoutdinov and Randall (2006) identified the primary mechanism for the transition from shallow to deep convection in the LBA case study to be the formation of cold pools in the BL through evaporating precipitation. Here, we examine the representation of the BL structures and consequent cloud development during the deep convection stage from the different schemes at the two main resolutions of interest, $\Delta x = 400$ m and 800 m. Following Khairoutdinov and Randall (2006), Figure 10 shows the moist static energy at height $z = 500$ m in the BL, superimposing the position of clouds near cloud base ($z = 1{,}200$ m). Moist static energy h is calculated as

$$h = c_p T + L_v q_v + gz, \tag{39}$$

where T is the absolute temperature, c_p is the specific heat of air for constant pressure, L_v the latent heat of vaporisation, and g is gravitational acceleration.

Figure 10a depicts larger than typical CBL coherent structures due to the cold-pool dynamics in the middle of the BL for the LES run. The cold pools, produced by negatively buoyant air, can be seen as areas of low h compared with the higher moist static energy of the ascending BL cells. Clouds are found on the edge of the cold gust front which results from the strong downdraft originating from precipitation evaporation above the BL (see Khairoutdinov & Randall, 2006; Kurowski *et al.*, 2018). Interestingly, coarser resolution SMAG runs produce a much more diffused picture of h (Figure 10b,e), which leads to less convective organisation, especially for the SMAG 800 m run (Figure 10e). Both dynamic simulations

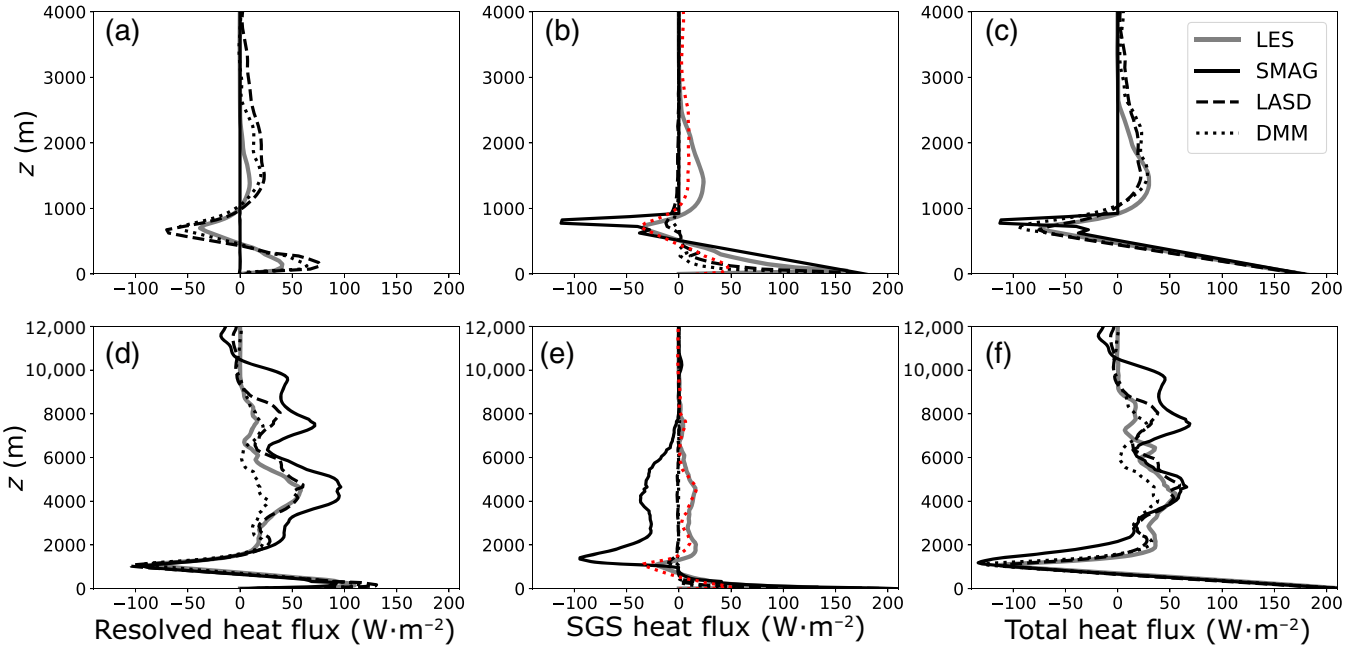

FIGURE 8 Planar-averaged profiles of (a, d) resolved heat flux, (b, e) subgrid-scale (SGS) heat flux from eddy-diffusion terms, (c, f) total (resolved + SGS) heat flux during the (a)–(c) shallow cumulus stage and (d)–(f) deep convection phase at $\Delta x = 400$ m from the conventional Smagorinsky (SMAG) model, the Lagrangian-averaged, dynamic Smagorinsky (LASD) model, and the Dynamic Mixed Model (DMM) simulations. The grey line in (a) and (d) represents the resolved heat flux and in (b) and (e) the SGS heat fluxes of the coarse-grained large-eddy simulation (LES) fields at the same scale. The red dotted line in (b) and (e) represents the SGS heat flux contribution from the DMM similarity terms, and the black dotted line represents the contribution from the (dynamic) Smagorinsky part of the DMM only.

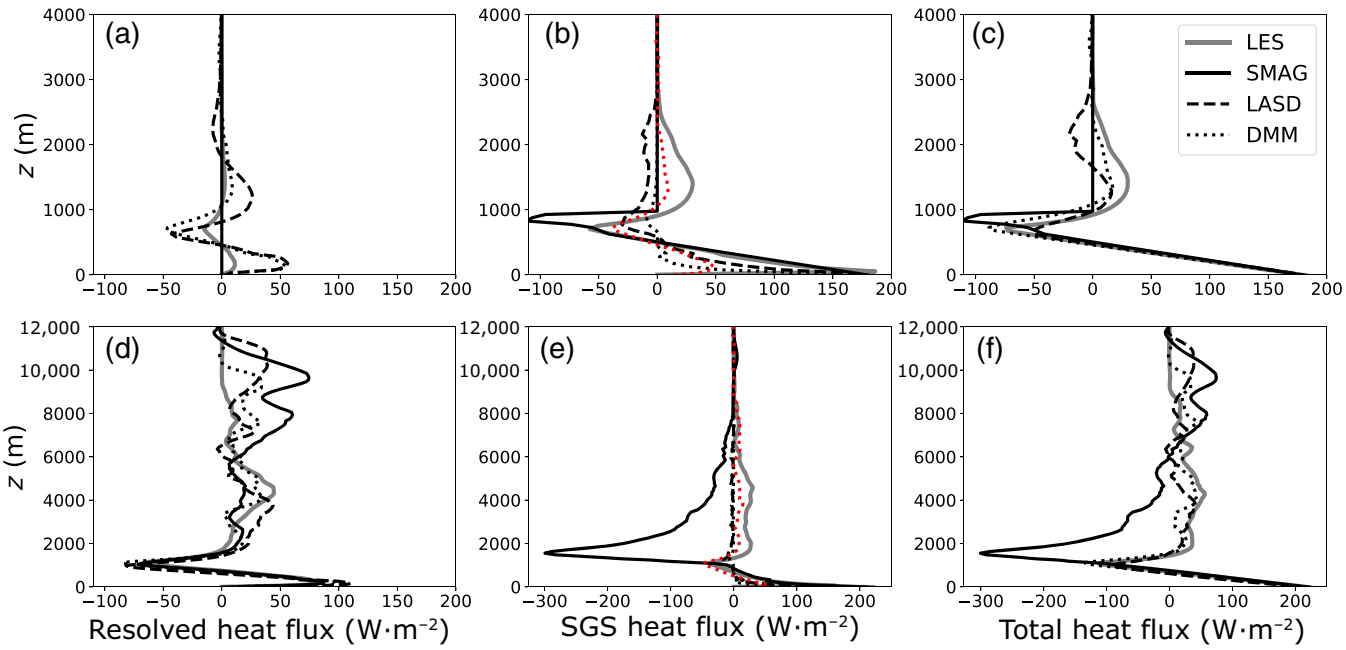

FIGURE 9 Same as Figure 8 but for the $\Delta x = 800$ m simulations.

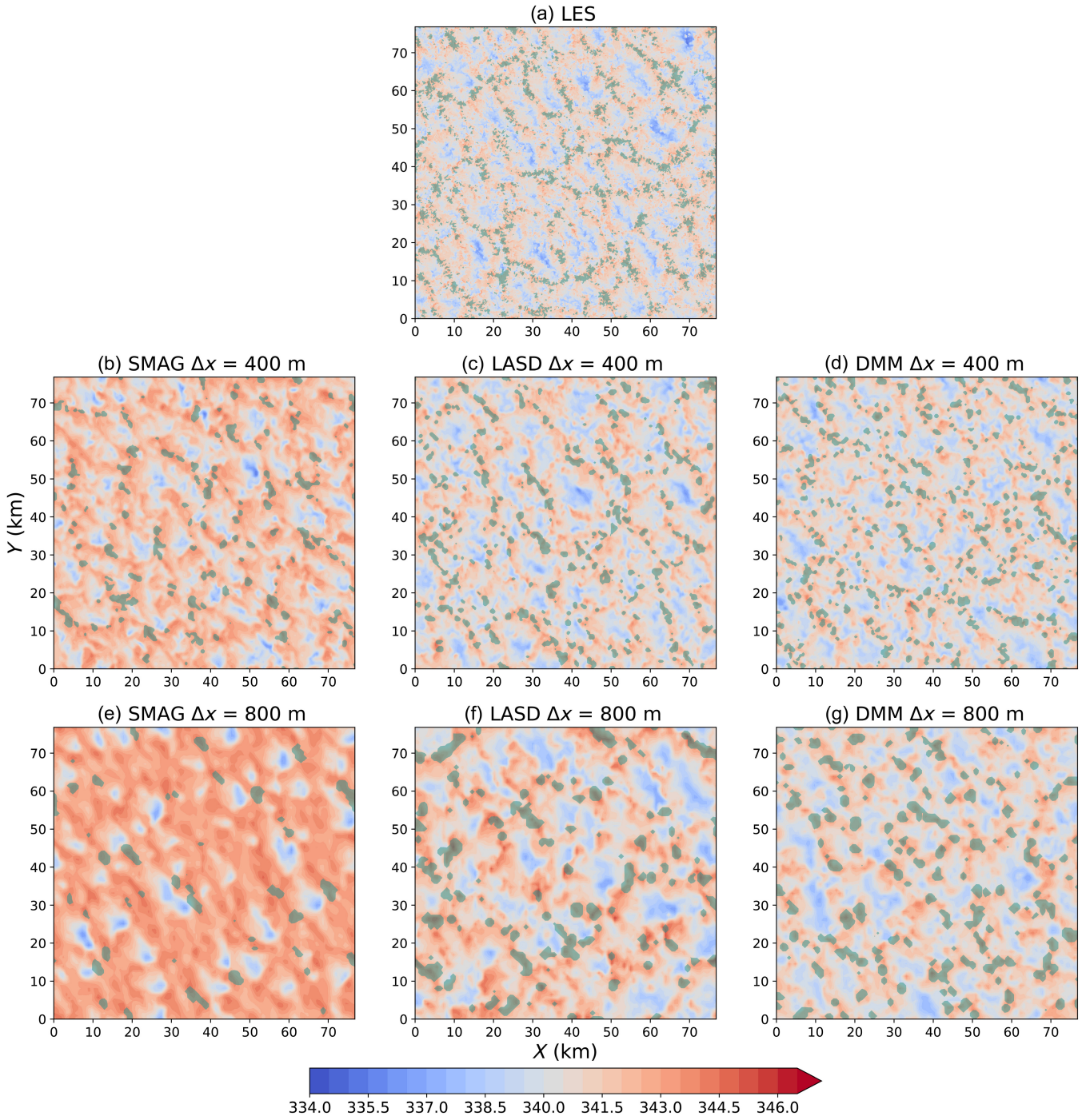

FIGURE 10 Horizontal cross-section of moist static energy h, with colour bar expressed in K (h/c_p), at a height of $z = 500$ m and $t = 21{,}300$ s for (a) large-eddy simulation (LES), (b, e) conventional Smagorinsky (SMAG) model, (c, f) the Lagrangian-averaged, dynamic Smagorinsky (LASD) model, and (d, g) Dynamic Mixed Model (DMM) at (b)–(d) $\Delta x = 400$ m and (e)–(g) $\Delta x = 800$ m. The transparent dark green filled contours denote cloudy areas (where $q_l \geq 10^{-5}$ g·g^{-1}) at $z = 1{,}200$ m.

(LASD and DMM) maintain a more detailed cold-pool structure, qualitatively closer to the LES even at 800 m (Figure 10f,g), with the LASD run (Figure 10f) remaining somewhat intermediate in between SMAG and DMM in accordance with the analysis of convection evolution noted earlier herein.

4 | IMPACT OF SIMILARITY TERMS ON THE SGS HYDROMETEOR FLUXES

The DMM simulations presented earlier herein were performed by only including the similarity terms in the SGS

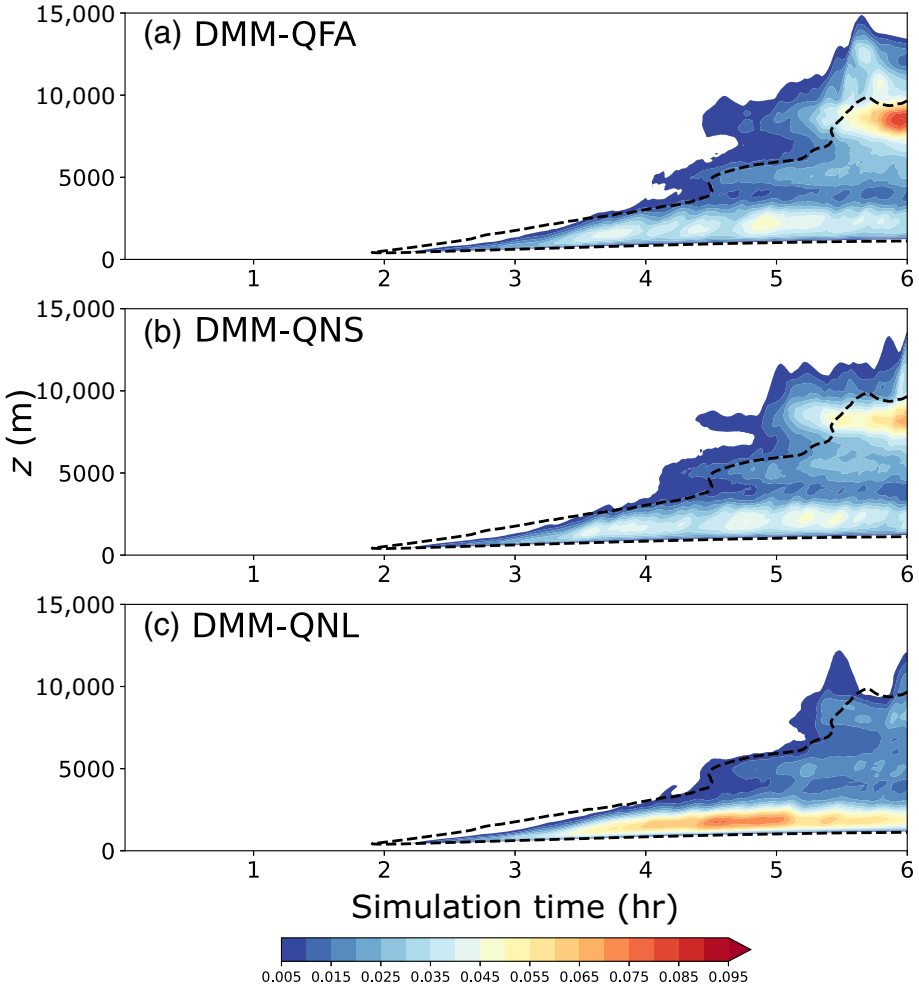

FIGURE 11 Time evolution of planar-averaged total condensate except rain (colour bar in g·kg^{-1}) from the (a) DMM-QFA, (b) DMM-QNS and (c) DMM-QNL sensitivity simulations at $\Delta x = 800$ m. The black dashed line shows the 0.005 g·kg^{-1} contour from the large-eddy simulation. DMM: Dynamic Mixed Model; QFA: using similarity terms in all water species; QNS: all similarity terms except for snow SGS flux; QNL: all similarity terms except for liquid water SGS flux.

heat flux equation, Equation (35). Here, we examine the impact of also adding the similarity terms to the water species SGS flux equations, following Equation (36). Sensitivity simulations were conducted at $\Delta x = 800$ m using the similarity terms in all water species (DMM-QFA), or in all except for the snow SGS flux (DMM-QNS), or in all except for the liquid water SGS flux (DMM-QNL). It should be noted that differences amongst these sensitivity simulations can also be seen at higher resolutions (especially at 400 m); however, they are more pronounced at 800 m.

Figure 11 shows the time evolution of condensate for the DMM-QFA, DMM-QNS, and DMM-QNL simulations. All of the simulations exhibit similar behaviour. The most pronounced difference is the reduced cloud liquid water in shallow clouds that translates to more ice condensate in the DMM-QFA compared with LES (Figure 1) and the control DMM (Figure 2i). Turning off the similarity terms in the snow SGS fluxes (DMM-QNS) does not significantly impact the time evolution or the vertical distribution of condensate, as seen in Figure 11b (the same applies for the graupel SGS fluxes but not shown here as snow is more abundant in the 800 m simulation). However, a marked impact comes from turning off the similarity terms in the liquid water SGS fluxes (DMM-QNL), resulting in a time evolution very similar to LES and DMM. It should be noted that no substantial differences in the precipitation rates or maximum w were found amongst the DMM and the sensitivity runs and, therefore, they are not shown here.

The differences between the liquid water and ice condensate mixing ratios from the sensitivity simulations and the LES are shown in Figure 12 for the shallow and deep cumulus phases. DMM-QFA and DMM-QNS show less q_l and substantially more frozen condensate ($q_s + q_g + q_i$) compared with the LES. DMM and DMM-QNL exhibit very similar behaviour to each other and are much closer to the LES profiles. This may be attributed to the liquid water SGS fluxes, which are strongly diverging in the shallow cumulus layer (as seen in Figure 13) and overexcessively transporting liquid water, which in turn evaporates above the cumulus layer, increasing the vapour content. The increased q_v in DMM-QFA compared with DMM can be seen in Figure 14 and is more pronounced during the deep cumulus phase, whereas the higher vapour values in

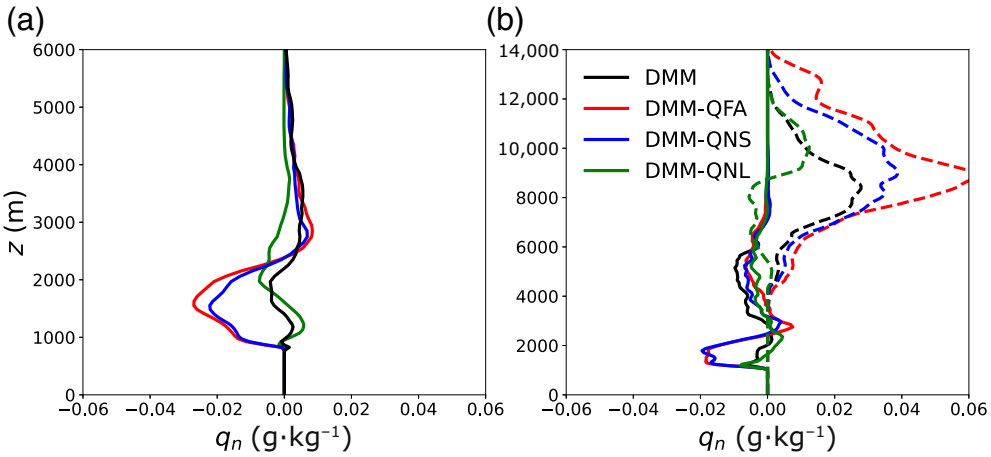

FIGURE 12 Planar-averaged differences between the individual sensitivity simulations and the large-eddy simulation (LES) profiles for q_l (solid lines) and frozen condensate $q_s + q_i + q_g$ (dashed lines) during (a) the shallow cumulus and (b) the deep stage. Note that there is no frozen condensate in (a). See legend for identifying the different simulations.

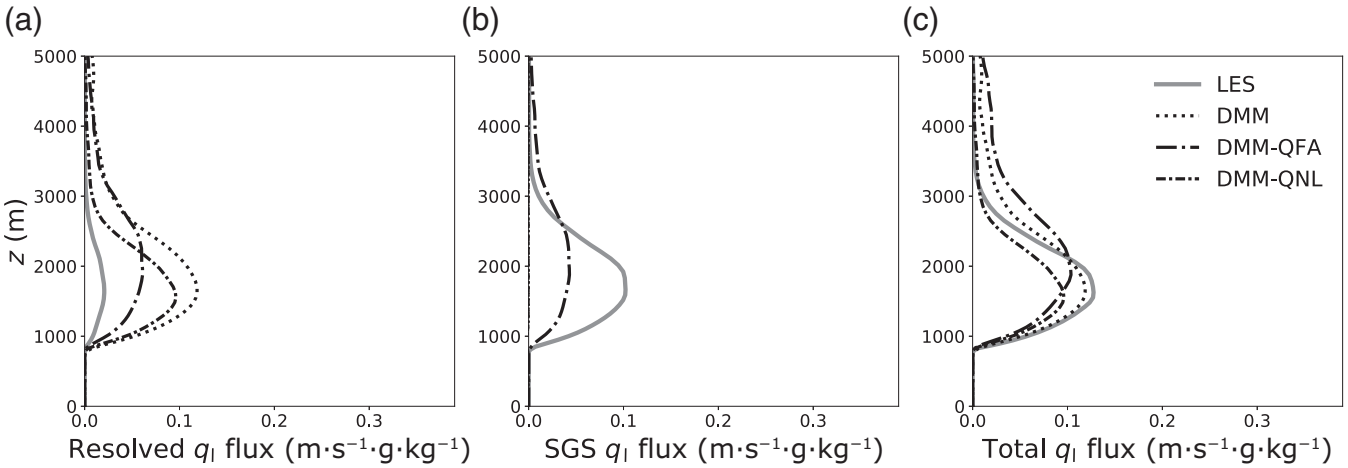

FIGURE 13 (a) Resolved, (b) subgrid-scale (SGS), and (c) total (resolved + SGS) liquid water fluxes from the sensitivity simulations at $\Delta x = 800$ m during the shallow cumulus stage. The grey lines in (a) and (b) represent the coarse-grained large-eddy simulation (LES) at 800 m, whereas that in (c) depicts the total LES flux.

the BL for DMM are related to the absence of this extra moisture transport from the SGS similarity terms.

Water vapour drives the strong snow growth through vapour deposition in the DMM-QFA simulations. To test this interpretation, the water vapour production rate due to evaporation/condensation during the shallow cumulus stage and the net snow production rate from vapour deposition (deposition minus sublimation) at the deep convection stage are presented in Figure 15. DMM-QNS is not presented here for clarity as it produces very similar profiles to the DMM-QFA run. Deposition is the dominant snow production mechanism in this case. DMM-QFA exhibits higher liquid water evaporation at the top of the cumulus layer and less condensation at cloud base. It also has almost double the snow production rates of DMM and DMM-QNL, which have very similar values for these q_v and q_s process rates.

Moreover, the total liquid water SGS fluxes in DMM-QFA are almost equally contributed between the resolved part and the similarity fluxes, which are able to reproduce the profile of the coarse-grained SGS fluxes (see Figure 13b). However, the total fluxes are more divergent compared with the LES, as can be seen in Figure 13c. Turning off only the similarity liquid water fluxes (DMM-QNL) results in SGS water flux vertical profiles very similar to the DMM that closely follows the LES.

5 | DISCUSSION AND CONCLUSIONS

CRMs have been traditionally used for process studies and parametrisation development, and the recent increase in computing power means that they can now be used

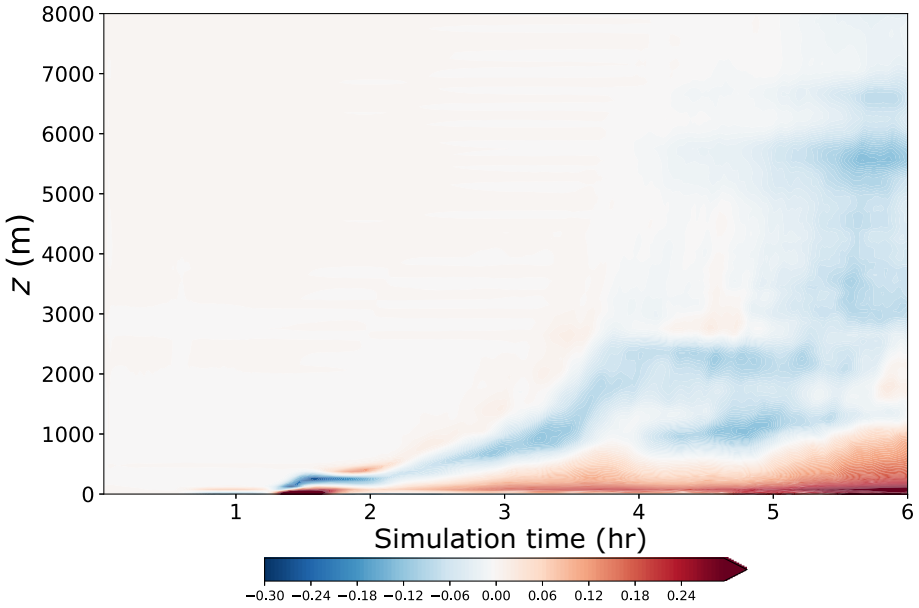

FIGURE 14 Time evolution of planar-averaged $\overline{q}_v$ differences (colour bar in g·kg^{-1}) between the DMM and DMM-QFA simulations at $\Delta x = 800$ m.

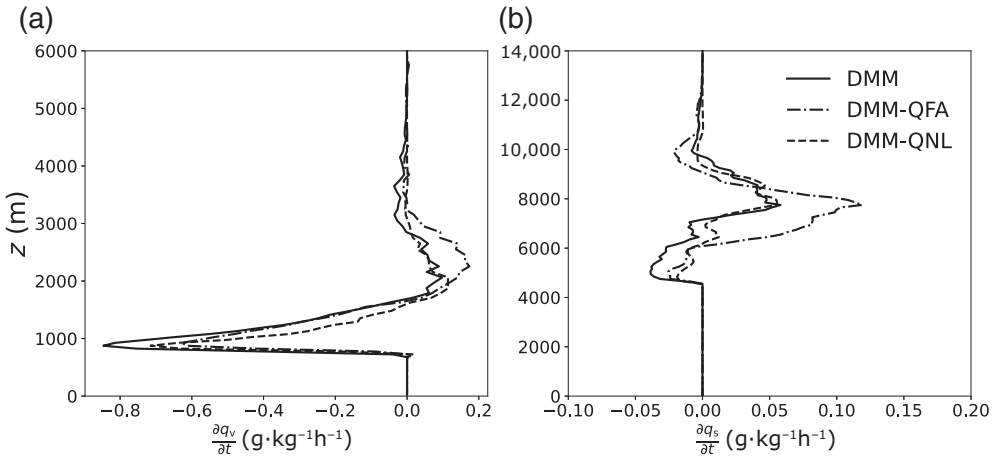

FIGURE 15 Planar-averaged tendencies of (a) $\overline{q}_v$ due to evaporation/condensation during the shallow cumulus stage and (b) $\overline{q}_s$ from net vapour deposition (deposition minus sublimation) during the deep stage for the sensitivity simulations ($\Delta x = 800$ m).

operationally for NWP. However, as has become evident in this study, the turbulence grey zone imposes significant challenges for the representation of the development of shallow and deep convection at sub-kilometre resolutions. Conventional 3D turbulence models have been shown to outperform one-dimensional mesoscale schemes especially in kilometre- to sub-kilometre-scale simulations of deep convection (e.g., Fiori *et al.*, 2010). Nonetheless, the SMAG scheme is unable to capture the shallow cumulus stage completely, with problems evident starting with the 200 m simulation and coarser (as also seen in Shi *et al.*, 2019). This leads to significant CAPE build-up that results in an unrealistic, instantaneous release of convective energy with excessive rainfall that misrepresents the deep convection phase of the LBA simulation.

During the diurnal development of convection, the flow passes through multiple grey-zone regimes depending on Λ/Δ (Chow *et al.*, 2019; Honnert *et al.*, 2011). The CBL development and shallow cumulus convection stage is dominated by the overdissipative nature of conventional schemes (i.e., SMAG) that leads to late spin-up of resolved flow and inaccurate representation of the CBL as the non-local fluxes are not properly accounted for due to the poorly resolved thermals (see e.g., Efstathiou, 2023). This results in completely missing the shallow cumulus stage, going straight to deep convection. In the deep cumulus stage the situation reverses, with the SMAG simulations demonstrating insufficient mixing, causing almost undilute and overly energetic deep clouds (Verrelle *et al.*, 2015). In addition, resolution convergence issues become evident, manifested by a non-monotonic transition of vertical velocity across the scales with maximum values at grey-zone resolutions.

Adopting a dynamically derived, scale-dependent length scale in LASD substantially improves the representation of convection transition, retaining the shallow stage in all simulations performed at grey-zone resolutions. As shown in other studies (Efstathiou, 2023; Efstathiou

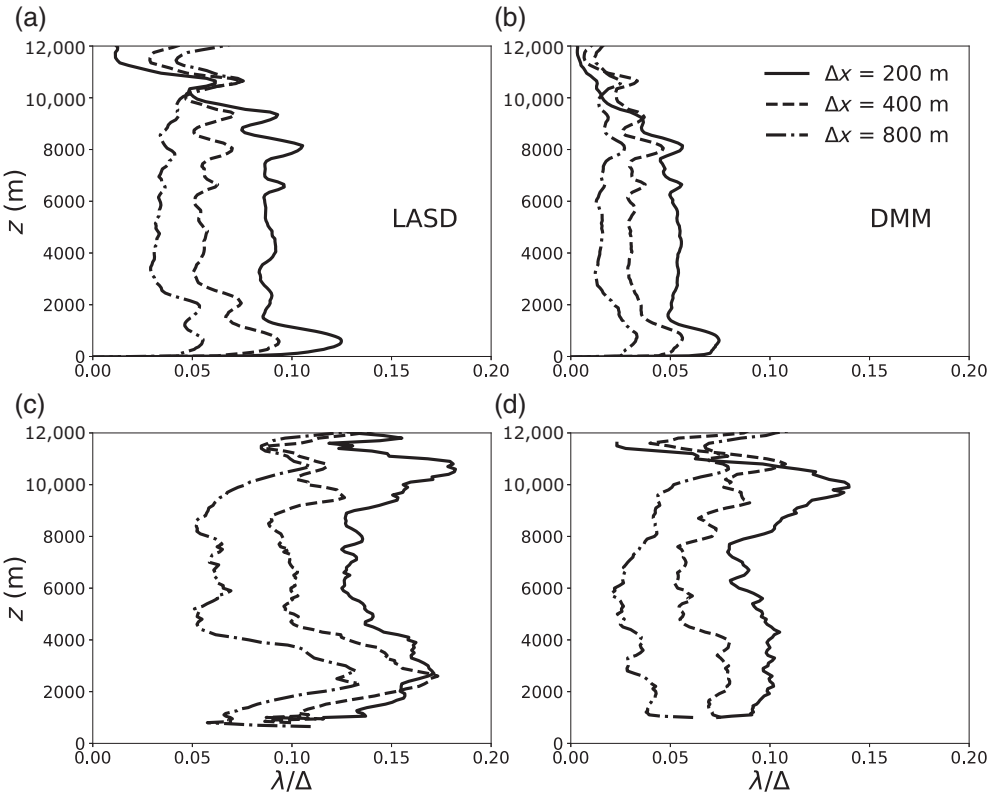

FIGURE 16
Planar-averaged λ/Δ profiles during the deep convection stage of the Large-Scale Biosphere–Atmosphere experiment (LBA) simulations with $\Delta x = 200$, 400, and 800 m for the (a) the Lagrangian-averaged, dynamic Smagorinsky (LASD) model and (b) Dynamic Mixed Model (DMM) simulations. Also shown are in-cloud ($q_l > 10^{-5}$ g·g^{-1}) averaged λ/Δ values for (c) LASD and (d) DMM.

et al., 2018), the dynamic approach is able to relax the basic assumptions behind the SMAG scheme, resulting in a scale-dependent behaviour in the grey zone that adapts to the partially resolved motions. Nonetheless, convection becomes more energetic at coarser resolutions and the duration of the shallow stage is reduced, exhibiting similar issues seen in the SMAG runs during the deep stage, especially in the 800 m simulation. The lack of any non-local SGS fluxes means that LASD simulations rely solely on the resolved flow to capture the non-local transports in the BL and cloud layer, which leads to overenergetic flow at coarser resolutions (see also Efstathiou, 2023).

The combination of the dynamic Smagorinsky approach with the similarity (Leonard) terms in the DMM scheme is able to reproduce LES characteristics across the grey-zone scales by optimising the eddy-viscosity (local) part of the scheme to the presence of the similarity terms. This can be seen in Figure 16, where the planar-averaged vertical profiles and the in-cloud averaged C_S ($C_S = \lambda/\Delta$) from the LASD and DMM simulations are shown. LASD has consistently larger values in the BL and cloud layer compared with the DMM, which includes the extra similarity terms. Both exhibit larger in-cloud length-scale values than the planar averaged profiles do, which is associated with the stronger in-cloud intensity of turbulence. The dynamic approach adapts to the additional SGS fluxes in DMM by producing different mixing-length profiles in the cloud layer and reducing the contribution of the dynamic Smagorinsky part of the subgrid scheme. Furthermore, the diffusive part of the model becomes less relevant at coarse resolutions with most of the SGS fluxes being represented by the similarity terms (see Figures 8 and 9). Even though the Smagorinsky part of the DMM is not scale dependent in the traditional sense (i.e., C_S is calculated utilising information from the 2Δ scales only) it includes information from the 4Δ scales through the filtering of the similarity terms.

Turbulence models with a dynamic derivation of the Pr number (C_θ) have been found to produce almost no eddy diffusion fluxes in the cloud layer (Efstathiou, 2023; Shi *et al.*, 2018, 2019) where turbulent transport is essentially non-local and counter-gradient. DMM is able to reproduce counter-gradient fluxes through the similarity terms that provide a form of backscatter, feeding energy back to the resolved scales and producing the necessary variability to capture convection development (Shi *et al.*, 2018). As also mentioned in Efstathiou (2023), the inability of a purely dissipative eddy-viscosity scheme to reproduce the counter-gradient fluxes limits the applicability of LASD in very coarse grey-zone resolutions.

Including the similarity terms only in the SGS heat flux equation enables DMM to reproduce the correct thermodynamic structure of the atmosphere, as well as transport and mixing characteristics of the other scalars (water

vapour and hydrometeors) that are similar to LES. A sensitivity test was performed where the similarity terms were added for all water species (DMM-QFA). Adding the similarity terms for all water species results in slightly worse results, especially related to the hydrometeor evolution and distribution, although the domain-mean surface precipitation remains unaffected. This is due to the strong transport of liquid water by the similarity SGS fluxes, primarily during the shallow stage, that lead to enhanced evaporation and vapour transport to higher levels and later strong snow growth through vapour deposition. Thus, the test revealed strong interactions between microphysics and turbulent mixing. The full understanding of the observed model behaviour deserves more dedicated analysis, especially at grey-zone resolutions, but is outside the scope of this study.

Moreover, the sensitivity tests highlight the possible need for better optimisation of the model parameters through a dynamic procedure such as the inclusion of the second term C_n in Equation (31) (and $C_{n\theta}$ in Equations 35 and 36) in the dynamic procedure to derive both parameters. We attempted to dynamically diagnose both coefficients (not shown); however, our grey-zone simulations returned a consistently negative C_n value that produced unsatisfactory results, whereas close to LES resolutions we found $C_n \approx 1$. This issue within the grey zone was traced back to the fact that the trace of the second term in the Z_{ij} tensor, Equation (34), becomes larger than the first term, which results in tensor contractions that return negative values. The same behaviour was identified in Anderson and Meneveau (1999), who showed that as the spectra deviate from a clear inertial subrange the trace of Z_{ij} tends to negative values. In any case, the one-parameter DMM produces the closest representation of the LES, compared with LASD and SMAG, because the diffusive part can adapt to the presence of the extra similarity terms, as shown in Figure 16. In future work we aim to use the Taylor-expanded form of the similarity terms (Moeng *et al.*, 2010), where the aforementioned behaviour of the second coefficient is not as pronounced according to Anderson and Meneveau (1999). This will allow for more impactful tests of a two-parameter dynamic mixed model for deep convection simulations.

ACKNOWLEDGEMENTS

This work was supported by the UKRI Natural Environment Research Council (grant NE/T011351/1 and grant NE/X018164/1). For the purpose of open access, the authors have applied a Creative Commons Attribution (CC BY) license to any author accepted manuscript version arising from this submission. We acknowledge use of the Monsoon2 system, a collaborative facility supplied under the Joint Weather and Climate Research Programme, a strategic partnership between the Met Office and the Natural Environment Research Council.

DATA AVAILABILITY STATEMENT

The research data supporting this publication are provided within this paper.

ORCID

Georgios A. Efstathiou https://orcid.org/0000-0003-3469-8729
Robert S. Plant https://orcid.org/0000-0001-8808-0022

REFERENCES

Anderson, R. & Meneveau, C. (1999) Effects of the similarity model in finite-difference LES of isotropic turbulence using a Lagrangian dynamic mixed model. *Flow, Turbulence and Combustion*, 62, 201–225. Available from: https://doi.org/10.1023/A:1009967228812

Bardina, J., Ferziger, J.H. & Reynolds, W.C. (1983) *Improved turbulence models based on large eddy simulation of homogeneous, incompressible turbulent flows*. Tech. Rep. TF-19. Stanford University. https://ntrs.nasa.gov/api/citations/19840009460/downloads/19840009460.pdf

Beare, R. (2014) A length scale defining partially-resolved boundary-layer turbulence simulations. *Boundary-Layer Meteorology*, 151, 39–55. Available from: https://doi.org/10.1007/s10546-013-9881-3

Bechtold, P., Chaboureau, J.-P., Beljaars, A., Betts, A.K., Köhler, M., Miller, M. et al. (2004) The simulation of the diurnal cycle of convective precipitation over land in a global model. *Quarterly Journal of the Royal Meteorological Society*, 130, 3119–3137 https://rmets.onlinelibrary.wiley.com/doi/abs/10.1256/qj.03.103

Betts, A.K., Fuentes, J.D., Garstang, M. & Ball, J.H. (2002) Surface diurnal cycle and boundary layer structure over rondônia during the rainy season. *Journal of Geophysical Research: Atmospheres*, 107, LBA 32–1–LBA 32–14 https://agupubs.onlinelibrary.wiley.com/doi/abs/10.1029/2001JD000356

Böing, S.J., Jonker, H.J.J., Siebesma, A.P. & Grabowski, W.W. (2012) Influence of the subcloud layer on the development of a deep convective ensemble. *Journal of the Atmospheric Sciences*, 69, 2682–2698 https://journals.ametsoc.org/view/journals/atsc/69/9/jas-d-11-0317.1.xml

Boutle, I.A., Eyre, J.E.J. & Lock, A.P. (2014) Seamless stratocumulus simulation across the turbulent gray zone. *Monthly Weather Review*, 142, 1655–1668. Available from: https://doi.org/10.1175/MWR-D-13-00229.1

Bou-Zeid, E., Meneveau, C. & Parlange, M. (2005) A scale-dependent Lagrangian dynamic model for large eddy simulation of complex turbulent flows. *Physics of Fluids*, 17(2), 025105. http://scitation.aip.org/content/aip/journal/pof2/17/2/10.1063/1.1839152

Brown, A.R. (1999) Large-eddy simulation and parametrization of the effects of shear on shallow cumulus convection. *Boundary-Layer Meteorology*, 91, 65–80. Available from: https://doi.org/10.1023/A:1001836612775

Brown, A.R., Cederwall, R.T., Chlond, A., Duynkerke, P.G., Golaz, J.-C., Khairoutdinov, M. et al. (2002) Large-eddy simulation of the diurnal cycle of shallow cumulus convection over land. *Quarterly Journal of the Royal Meteorological Society*, 128, 1075–1093 https://rmets.onlinelibrary.wiley.com/doi/abs/10.1256/003590002320373210

Brown, N., Lepper, A., Weiland, M., Hill, A., Shipway, B. & Maynard, C. (2015) A directive based hybrid Met Office NERC cloud model. Proceedings of the second workshop on accelerator programming using directives, WACCPD'15. New York, NY, USA: Association for Computing Machinery. https://doi.org/10.1145/2832105.2832115

Bryan, G.H., Wyngaard, J.C. & Fritsch, J.M. (2003) Resolution requirements for the simulation of deep moist convection. *Monthly Weather Review*, 131, 2394–2416 https://journals.ametsoc.org/view/journals/mwre/131/10/1520-0493_2003_131_2394_rrftso_2.0.co_2.xml

Chakraborty, A. (2010) The skill of ECMWF medium-range forecasts during the year of tropical convection 2008. *Monthly Weather Review*, 138, 3787–3805 https://journals.ametsoc.org/view/journals/mwre/138/10/2010mwr3217.1.xml

Chow, F.K., Schär, C., Ban, N., Lundquist, K.A., Schlemmer, L. & Shi, X. (2019) Crossing multiple gray zones in the transition from mesoscale to microscale simulation over complex terrain. *Atmosphere*, 10 https://www.mdpi.com/2073-4433/10/5/274

Clark, P., Roberts, N., Lean, H., Ballard, S.P. & Charlton-Perez, C. (2016) Convection-permitting models: a step-change in rainfall forecasting. *Meteorological Applications*, 23, 165–181 https://rmets.onlinelibrary.wiley.com/doi/abs/10.1002/met.1538

Efstathiou, G.A. (2023) Dynamic subgrid turbulence modeling for shallow cumulus convection simulations beyond LES resolutions. *Journal of the Atmospheric Sciences*, 80, 1519–1545 https://journals.ametsoc.org/view/journals/atsc/80/6/JAS-D-22-0132.1.xml

Efstathiou, G.A., Beare, R.J., Osborne, S. & Lock, A.P. (2016) Grey zone simulations of the morning convective boundary layer development. *Journal of Geophysical Research: Atmospheres*, 121, 4769–4782. Available from: https://doi.org/10.1002/2016JD024860.2016JD024860

Efstathiou, G.A., Plant, R.S. & Bopape, M.M. (2018) Simulation of an evolving convective boundary layer using a scale-dependent dynamic smagorinsky model at near-gray-zone resolutions. *Journal of Applied Meteorology and Climatology*, 57, 2197–2214 https://journals.ametsoc.org/view/journals/apme/57/9/jamc-d-17-0318.1.xml

Field, P.R., Hill, A., Shipway, B., Furtado, K., Wilkinson, J., Miltenberger, A. et al. (2023) Implementation of a double moment cloud microphysics scheme in the UK Met Office regional numerical weather prediction model. *Quarterly Journal of the Royal Meteorological Society*, 149(752), 703–739 https://rmets.onlinelibrary.wiley.com/doi/abs/10.1002/qj.4414

Fiori, E., Parodi, A. & Siccardi, F. (2010) Turbulence closure parameterization and grid spacing effects in simulated supercell storms. *Journal of the Atmospheric Sciences*, 67, 3870–3890 https://journals.ametsoc.org/view/journals/atsc/67/12/2010jas3359.1.xml

Germano, M. (1986) A proposal for a redefinition of the turbulent stresses in the filtered Navier–stokes equations. *The Physics of Fluids*, 29, 2323–2324 https://aip.scitation.org/doi/abs/10.1063/1.865568

Germano, M., Piomelli, U., Moin, P. & Cabot, W.H. (1991) A dynamic subgrid-scale eddy viscosity model. *Physics of Fluids A*, 3, 1760–1765 http://scitation.aip.org/content/aip/journal/pofa/3/7/10.1063/1.857955

Goger, B., Rotach, M.W., Gohm, A., Fuhrer, O., Stiperski, I. & Holtslag, A.A.M. (2018) The impact of three-dimensional effects on the simulation of turbulence kinetic energy in a major alpine valley. *Boundary-Layer Meteorology*, 168, 1–27. Available from: https://doi.org/10.1007/s10546-018-0341-y

Grabowski, W.W. (2023) Daytime convective development over land: the role of surface forcing. *Quarterly Journal of the Royal Meteorological Society*, 149, 2800–2819 https://rmets.onlinelibrary.wiley.com/doi/abs/10.1002/qj.4532

Grabowski, W.W., Bechtold, P., Cheng, A., Forbes, R., Halliwell, C., Khairoutdinov, M. et al. (2006) Daytime convective development over land: a model intercomparison based on LBA observations. *Quarterly Journal of the Royal Meteorological Society*, 132, 317–344 https://rmets.onlinelibrary.wiley.com/doi/abs/10.1256/qj.04.147

Griewank, P.J., Heus, T., Lareau, N.P. & Neggers, R.A.J. (2020) Size dependence in chord characteristics from simulated and observed continental shallow cumulus. *Atmospheric Chemistry and Physics*, 20, 10211–10230 https://acp.copernicus.org/articles/20/10211/2020/

Gu, J.-F., Plant, R.S., Holloway, C.E., Jones, T.R., Stirling, A., Clark, P.A. et al. (2020) Evaluation of the bulk mass flux formulation using large-eddy simulations. *Journal of the Atmospheric Sciences*, 77, 2115–2137 https://journals.ametsoc.org/view/journals/atsc/77/6/JAS-D-19-0224.1.xml

Hanley, K., Whitall, M., Stirling, A. & Clark, P. (2019) Modifications to the representation of subgrid mixing in kilometre-scale versions of the unified model. *Quarterly Journal of the Royal Meteorological Society*, 145, 3361–3375 https://rmets.onlinelibrary.wiley.com/doi/abs/10.1002/qj.3624

Hanley, K.E., Plant, R.S., Stein, T.H.M., Hogan, R.J., Nicol, J.C., Lean, H.W. et al. (2015) Mixing-length controls on high-resolution simulations of convective storms. *Quarterly Journal of the Royal Meteorological Society*, 141, 272–284. Available from: https://doi.org/10.1002/qj.2356

Honnert, R., Efstathiou, G.A., Beare, R.J., Ito, J., Lock, A., Neggers, R. et al. (2020) The atmospheric boundary layer and the "gray zone" of turbulence: a critical review. *Journal of Geophysical Research: Atmospheres*, 125, e2019JD030317. Available from: https://doi.org/10.1029/2019JD030317

Honnert, R., Masson, V. & Couvreux, F. (2011) A diagnostic for evaluating the representation of turbulence in atmospheric models at the kilometric scale. *Journal of the Atmospheric Sciences*, 68, 3112–3131. Available from: https://doi.org/10.1175/JAS-D-11-061.1

Huang, H.-Y., Stevens, B. & Margulis, S.A. (2008) Application of dynamic subgrid-scale models for large-eddy simulation of the daytime convective boundary layer over heterogeneous surfaces. *Boundary-Layer Meteorology*, 126, 327–348. Available from: https://doi.org/10.1007/s10546-007-9239-9

Ito, J., Hayashi, S., Hashimoto, A., Ohtake, H., Uno, F., Yoshimura, H. et al. (2017) Stalled improvement in a numerical weather prediction model as horizontal resolution increases to the sub-kilometer scale. *Scientific Online Letters on the Atmosphere*, 13, 151–156.

Khairoutdinov, M. & Randall, D. (2006) High-resolution simulation of shallow-to-deep convection transition over land. *Journal of the Atmospheric Sciences*, 63, 3421–3436 https://journals.ametsoc.org/view/journals/atsc/63/12/jas3810.1.xml

Kidd, C., Dawkins, E. & Huffman, G. (2013) Comparison of precipitation derived from the ECMWF operational forecast model and satellite precipitation datasets. *Journal of Hydrometeorology*, 14, 1463–1482 https://journals.ametsoc.org/view/journals/hydr/14/5/jhm-d-12-0182_1.xml

Kirkpatrick, M.P., Ackerman, A.S., Stevens, D.E. & Mansour, N.N. (2006) On the application of the dynamic Smagorinsky model to large-eddy simulations of the cloud-topped atmospheric boundary layer. *Journal of the Atmospheric Sciences*, 63, 526–546. Available from: https://doi.org/10.1175/JAS3651.1

Krishna, U.V.M., Das, S.K., Deshpande, S.M. & Pandithurai, G. (2021) Physical processes controlling the diurnal cycle of convective storms in the Western Ghats. *Scientific Reports*, 11, 14103. Available from: https://doi.org/10.1038/s41598-021-93173-0

Krishnamurti, T.N., Gnanaseelan, C. & Chakraborty, A. (2007) Prediction of the diurnal change using a multimodel superensemble. Part I: Precipitation. *Monthly Weather Review*, 135, 3613–3632 https://journals.ametsoc.org/view/journals/mwre/135/10/mwr3446.1.xml

Kurowski, M.J., Suselj, K., Grabowski, W.W. & Teixeira, J. (2018) Shallow-to-deep transition of continental moist convection: cold pools, surface fluxes, and mesoscale organization. *Journal of the Atmospheric Sciences*, 75, 4071–4090 https://journals.ametsoc.org/view/journals/atsc/75/12/jas-d-18-0031.1.xml

Kurowski, M.J. & Teixeira, J. (2018) A scale-adaptive turbulent kinetic energy closure for the dry convective boundary layer. *Journal of the Atmospheric Sciences*, 75, 675–690 https://journals.ametsoc.org/view/journals/atsc/75/2/jas-d-16-0296.1.xml

Lancz, D., Szintai, B. & Honnert, R. (2018) Modification of a parametrization of shallow convection in the grey zone using a mesoscale model. *Boundary-Layer Meteorology*, 169, 483–503. Available from: https://doi.org/10.1007/s10546-018-0375-1

Lang, S., Tao, W.-K., Simpson, J., Cifelli, R., Rutledge, S., Olson, W. et al. (2007) Improving simulations of convective systems from TRMM LBA: easterly and westerly regimes. *Journal of the Atmospheric Sciences*, 64, 1141–1164 https://journals.ametsoc.org/view/journals/atsc/64/4/jas3879.1.xml

Lilly, D.K. (1967) The representation of small-scale turbulence in numerical simulation experiments. Proc. IBM scientific computing Symp. On environmental sciences, 195.

Lilly, D.K. (1992) A proposed modification of the Germano subgrid-scale closure method. *Physics of Fluids A: Fluid Dynamics*, 4, 633–635. Available from: https://doi.org/10.1063/1.858280

Liu, S., Meneveau, C. & Katz, J. (1994) On the properties of similarity subgrid-scale models as deduced from measurements in a turbulent jet. *Journal of Fluid Mechanics*, 275, 83–119.

Mason, P.J. & Thomson, D.J. (1992) Stochastic backscatter in large-eddy simulations of boundary layers. *Journal of Fluid Mechanics*, 242, 51–78 https://www.cambridge.org/core/article/stochastic-backscatter-in-large-eddy-simulations-of-boundary-layers/8DA0CAA88C4B9B841FA8887E12685312

Matheou, G., Chung, D., Nuijens, L., Stevens, B. & Teixeira, J. (2011) On the fidelity of large-eddy simulation of shallow precipitating cumulus convection. *Monthly Weather Review*, 139, 2918–2939 https://journals.ametsoc.org/view/journals/mwre/139/9/2011mwr3599.1.xml

Meneveau, C., Lund, T.S. & Cabot, W.H. (1996) A Lagrangian dynamic subgrid-scale model of turbulence. *Journal of Fluid Mechanics*, 319, 353–385.

Moeng, C.-H., Sullivan, P.P., Khairoutdinov, M.F. & Randall, D.A. (2010) A mixed scheme for subgrid-scale fluxes in cloud-resolving models. *Journal of the Atmospheric Sciences*, 67, 3692–3705 https://journals.ametsoc.org/view/journals/atsc/67/11/2010jas3565.1.xml

Nakanishi, M. & Niino, H. (2009) Development of an improved turbulence closure model for the atmospheric boundary layer. *Journal of the Meteorological Society of Japan. Series II*, 87, 895–912.

Petch, J.C., Brown, A.R. & Gray, M.E.B. (2002) The impact of horizontal resolution on the simulations of convective development over land. *Quarterly Journal of the Royal Meteorological Society*, 128, 2031–2044 https://rmets.onlinelibrary.wiley.com/doi/abs/10.1256/003590002320603511

Porté-Agel, F., Meneveau, C. & Parlange, M.B. (2000) A scale-dependent dynamic model for large-eddy simulation: application to a neutral atmospheric boundary layer. *Journal of Fluid Mechanics*, 415, 261–284 http://journals.cambridge.org/article_S0022112000008776

Rai, R.K., Berg, L.K., Kosović, B., Haupt, S.E., Mirocha, J.D., Ennis, B.L. et al. (2019) Evaluation of the impact of horizontal grid spacing in terra incognita on coupled mesoscale–microscale simulations using the WRF framework. *Monthly Weather Review*, 147, 1007–1027 https://journals.ametsoc.org/view/journals/mwre/147/3/mwr-d-18-0282.1.xml

Schär, C., Fuhrer, O., Arteaga, A., Ban, N., Charpilloz, C., Girolamo, S.D. et al. (2020) Kilometer-scale climate models: prospects and challenges. *Bulletin of the American Meteorological Society*, 101, E567–E587 https://journals.ametsoc.org/view/journals/bams/101/5/bams-d-18-0167.1.xml

Shi, X., Chow, F.K., Street, R.L. & Bryan, G.H. (2019) Key elements of turbulence closures for simulating deep convection at kilometer-scale resolution. *Journal of Advances in Modeling Earth Systems*, 11, 818–838 https://agupubs.onlinelibrary.wiley.com/doi/abs/10.1029/2018MS001446

Shi, X., Hagen, H.L., Chow, F.K., Bryan, G.H. & Street, R.L. (2018) Large-eddy simulation of the stratocumulus-capped boundary layer with explicit filtering and reconstruction turbulence modeling. *Journal of the Atmospheric Sciences*, 75, 611–637 https://journals.ametsoc.org/view/journals/atsc/75/2/jas-d-17-0162.1.xml

Shin, H.H. & Hong, S.-Y. (2015) Representation of the subgrid-scale turbulent transport in convective boundary layers at gray-zone resolutions. *Monthly Weather Review*, 143, 250–271. Available from: https://doi.org/10.1175/MWR-D-14-00116.1

Simon, J.S., Zhou, B., Mirocha, J.D. & Chow, F.K. (2019) Explicit filtering and reconstruction to reduce grid dependence in convective boundary layer simulations using WRF-LES. *Monthly Weather Review*, 147, 1805–1821 https://journals.ametsoc.org/view/journals/mwre/147/5/mwr-d-18-0205.1.xml

Singh, S., Kalthoff, N. & Gantner, L. (2021) Sensitivity of convective precipitation to model grid spacing and land-surface resolution in ICON. *Quarterly Journal of the Royal Meteorological Society*, 147, 2709–2728 https://rmets.onlinelibrary.wiley.com/doi/abs/10.1002/qj.4046

Smagorinsky, J. (1963) General circulation experiments with the primitive equations. *Monthly Weather Review*, 91, 99–164. Available from: https://doi.org/10.1175/1520-0493(1963)091<0099:GCEWTP>2.3.CO;2

Stevens, B., Moeng, C.-H., Ackerman, A.S., Bretherton, C.S., Chlond, A., de Roode, S. et al. (2005) Evaluation of large-eddy simulations via observations of nocturnal marine stratocumulus. *Monthly Weather Review*, 133, 1443–1462 https://journals.ametsoc.org/view/journals/mwre/133/6/mwr2930.1.xml

Strauss, C., Ricard, D., Lac, C. & Verrelle, A. (2019) Evaluation of turbulence parametrizations in convective clouds and their environment based on a large-eddy simulation. *Quarterly Journal of the Royal Meteorological Society*, 145, 3195–3217 https://rmets.onlinelibrary.wiley.com/doi/abs/10.1002/qj.3614

Verrelle, A., Ricard, D. & Lac, C. (2015) Sensitivity of high-resolution idealized simulations of thunderstorms to horizontal resolution and turbulence parametrization. *Quarterly Journal of the Royal Meteorological Society*, 141, 433–448 https://rmets.onlinelibrary.wiley.com/doi/abs/10.1002/qj.2363

Verrelle, A., Ricard, D. & Lac, C. (2017) Evaluation and improvement of turbulence parameterization inside deep convective clouds at kilometer-scale resolution. *Monthly Weather Review*, 145, 3947–3967 https://journals.ametsoc.org/view/journals/mwre/145/10/mwr-d-16-0404.1.xml

Wyngaard, J.C. (2004) Toward numerical modeling in the "terra incognita". *Journal of the Atmospheric Sciences*, 61, 1816–1826. Available from: https://doi.org/10.1175/1520-0469(2004)061<1816:TNMITT>2.0.CO;2

Yuan, W., Yu, R., Zhang, M., Lin, W., Li, J. & Fu, Y. (2013) Diurnal cycle of summer precipitation over subtropical east Asia in CAM5. *Journal of Climate*, 26, 3159–3172 https://journals.ametsoc.org/view/journals/clim/26/10/jcli-d-12-00119.1.xml

Zang, Y., Street, R.L. & Koseff, J.R. (1993) A dynamic mixed subgrid-scale model and its application to turbulent recirculating flows. *Physics of Fluids A: Fluid Dynamics*, 5, 3186–3196. Available from: https://doi.org/10.1063/1.858675

Zhang, X., Bao, J.-W., Chen, B. & Grell, E.D. (2018) A three-dimensional scale-adaptive turbulent kinetic energy scheme in the WRF-ARW model. *Monthly Weather Review*, 146, 2023–2045 https://journals.ametsoc.org/view/journals/mwre/146/7/mwr-d-17-0356.1.xml

How to cite this article: Efstathiou, G.A., Plant, R.S. & Chow, F.K. (2024) Grey-zone simulations of shallow-to-deep convection transition using dynamic subgrid-scale turbulence models. *Quarterly Journal of the Royal Meteorological Society*, 150(764), 4306–4328. Available from: https://doi.org/10.1002/qj.4817

APPENDIX A. EXAMINING THE CONVERGENCE OF THE REFERENCE LBA LES

Figure A.1 compares the reference LES simulation ($\Delta x = 50$ m using Smagorinsky) with a $\Delta x = 100$ m Smagorinsky (SMAG) run in terms of the evolution of maximum w, mean surface precipitation, LWP, and IWP. Results show that the two simulations produce fairly similar time series with most differences seen in the spin-up and maximum attained values of w (Figure A.1a). However, these differences do not seem to have a pronounced impact on LWP or IWC, or, as a result, on the mean precipitation rate. Moreover, the evolution and magnitude of the mean precipitation rate in both runs is very close to Khairoutdinov and Randall (2006) and Grabowski *et al.* (2006). The same comment holds for LWP and IWC compared with Grabowski *et al.* (2006). Bearing in mind the difficulty of achieving convergence in deep convection simulations (see Bryan *et al.*, 2003) amongst different models (Grabowski *et al.*, 2006), our reference simulation shows consistency near the LES limit (see also Figure 1). Any uncertainties in our reference LES results are modest in comparison with the differences between the reference and grey-zone simulation results, and hence the reference simulation is fit for the purpose of judging the quality of the various grey-zone simulations.

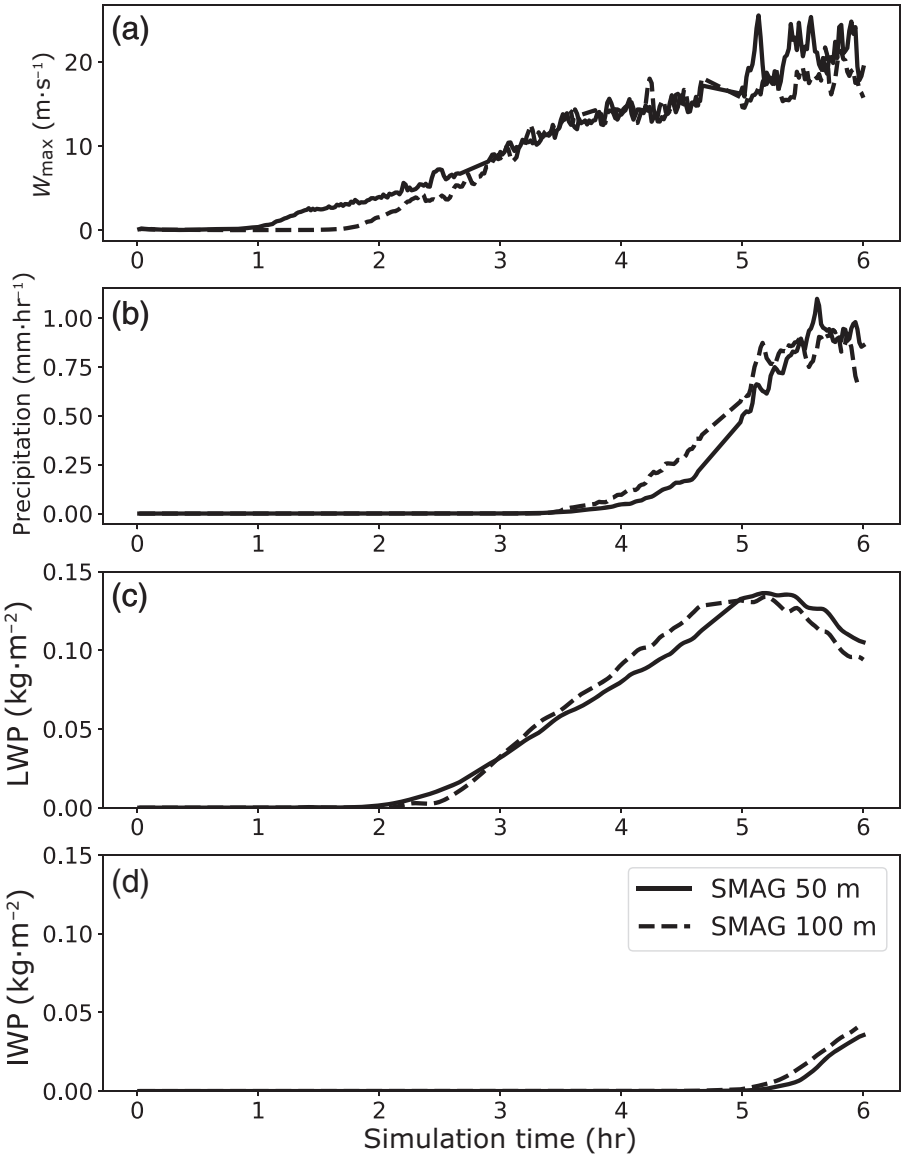

FIGURE A.1 Time evolution of (a) maximum vertical velocity, (b) mean precipitation rate, (c) mean liquid water path (LWP), and (d) mean ice water path (IWP) for the reference large-eddy simulation (SMAG $\Delta x = 50$ m) and a SMAG $\Delta x = 100$ m simulation. SMAG: conventional Smagorinsky model.